

Designer Meron Lattice on the Surface of a Topological Insulator

Daniele Guerzi,¹ Jie Wang,¹ J. H. Pixley,^{2,1} and Jennifer Cano^{3,1}

¹Center for Computational Quantum Physics, Flatiron Institute, New York, New York 10010, USA

²Department of Physics and Astronomy, Center for Materials Theory,
Rutgers University, Piscataway, New Jersey 08854, USA

³Department of Physics and Astronomy, Stony Brook University, Stony Brook, New York 11974, USA

We present a promising new route to realize spontaneous magnetic order on the surface of a 3D topological insulator by applying a superlattice potential. The superlattice potential creates tunable van Hove singularities, which, when combined with strong spin-orbit coupling and Coulomb repulsion give rise to a topological meron lattice spin texture. The periodicity of this designer meron lattice can be tuned by varying the periodicity of the superlattice potential. We characterize the magnetic order using Ginzburg-Landau theory and show that the magnetic transition temperature reaches experimentally accessible values. Our work introduces a new direction to realize exotic quantum order by engineering interacting Dirac electrons in a superlattice potential, with promising applications to spintronics.

Three-dimensional topological insulators (TIs) host gapless surface Dirac cones protected by time reversal symmetry [1–11]. In the presence of strong interactions, time-reversal symmetry can be spontaneously broken, gapping the Dirac cone. The result is an exotic magnetically ordered surface exhibiting the quantized anomalous Hall effect [5, 12–18]. However, for all measured TIs, the Coulomb interaction is too weak to induce the magnetically ordered phase [5, 12, 14, 18].

In this manuscript, we show that a superlattice potential provides a new and experimentally accessible route to realize spontaneous magnetic order on the surface of a TI as detailed in Fig. 1(a). The superlattice potential downfolds and strongly renormalizes the low-energy band structure, creating satellite Dirac cones without opening a gap [19] and inducing strong van Hove singularities (VHSs) [20]. We show that the superlattice induced VHSs drive a spin density wave instability that results in an exotic meron lattice with an accessible critical temperature T_c on the order of 1–10K. A meron, as shown in Fig. 1(b), is topologically equivalent to half a skyrmion: magnetic moments in its core point up or down, but magnetic moments along its boundary are in-plane, which makes it less stable than a skyrmion [21]. While topological spin textures such as skyrmions have been observed in non-centrosymmetric magnets [22–25], ultrathin magnetic films [26–28] and multiferroic insulators [29, 30], a meron lattice has only been observed recently [31, 32].

The meron lattice we describe on the surface of the TI is stabilized by the interplay between the superlattice potential and the strong spin-orbit coupling (SOC) on the TI surface that “locks” the spin to the momentum, forcing the magnetic moments to rotate in space about an in-plane axis. It features several novel aspects: (1) it leaves the surface Dirac cone gapless; (2) each unit cell exhibits two merons with opposite topological charge; and (3) the meron lattice periodicity is determined by the applied potential, *i.e.*, it can be chosen by design. These features make it distinct from other magnetic textures

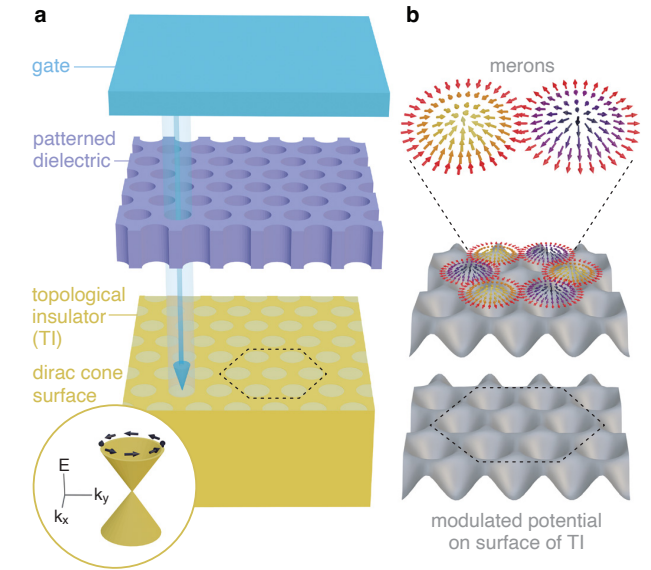


Figure 1. **Schematic of experimental setup and meron spin texture.** (a) The experiment consists, from top to bottom, of a metallic gate, a patterned dielectric, and a topological insulator. Applying a bias between the metallic gate and the topological insulator imposes a modulated potential on the surface of the TI. (b) Magnetization exhibiting a half-integer winding characteristic of a meron topological spin texture. In the magnetic phase, merons are pinned by the superlattice potential to form a meron lattice.

induced on [5, 12–18] or proximity-coupled [33–37] to the surface of a TI.

In this work we focus on the experimental setup shown in Fig. 1(a), which depicts a superlattice potential imposed on the surface of a TI by gating a patterned dielectric stacked above the TI surface. This approach was introduced to realize a superlattice potential on graphene with periodicity down to 35nm and strength $\sim 50\text{meV}$ [38, 39]. It offers great tunability: the periodicity, strength, and symmetry of the potential can be engineered. A superlattice potential has been stud-

ied theoretically to band engineer topological materials [19, 20, 40–47].

Model of an interacting TI surface.—We consider interacting electrons on the surface of a TI described by the Hamiltonian $\hat{H} = \hat{H}_0 + \hat{H}_{\text{int}}$. The non-interacting Hamiltonian $\hat{H}_0 = \int d^2\mathbf{r} \hat{\Psi}^\dagger(\mathbf{r}) H_0(\mathbf{r}) \hat{\Psi}(\mathbf{r})$ describes a spin-momentum locked Dirac cone subject to a superlattice potential,

$$H_0(\mathbf{r}) = v_F(-i\nabla_{\mathbf{r}} \times \boldsymbol{\sigma})_z + \sigma_0 w(\mathbf{r}), \quad (1)$$

where $\nabla_{\mathbf{r}} = (\partial_x, \partial_y)$, $\boldsymbol{\sigma} = (\sigma_x, \sigma_y, \sigma_z)$ are the Pauli matrices, σ_0 the identity, and $w(\mathbf{r}) = 2w \sum_{j=1}^3 \cos(\mathbf{q}_j \cdot \mathbf{r})$ is the hexagonal superlattice potential, with amplitude w and wave vectors $\mathbf{q}_{1,2,3}$ illustrated as red vectors in Fig. 2(a). The wave vectors satisfy $|\mathbf{q}_{1,2,3}| = 4\pi/\sqrt{3}L$, where L is the periodicity of the potential. We set the Fermi velocity to $v_F = 2.55\text{eV}\text{\AA}$, the experimentally measured value in Bi_2Te_3 [7, 8]. For the moment we neglect higher-order corrections [5] to the Dirac cone dispersion (1). Then Eq. (1) depends only on a single dimensionless parameter $w/(v_FL)$.

The Hamiltonian in Eq. (1) is invariant under time-reversal $T = \sigma_y K$, where K indicates complex conjugation, as well as a three-fold rotational symmetry, $C_{3z} = e^{2i\pi\sigma_z/3}$ and the mirror symmetries, $m_y = \sigma_y$ and $m_x = \sigma_x$, which act on both spin and spatial coordinates. Combinations of these imply invariance under two- and six-fold rotation symmetries, $C_{2z} = i\sigma_z$, $C_{6z} = e^{-i\pi\sigma_z/6}$, respectively. The potential $w(\mathbf{r})$ breaks particle-hole symmetry.

The superlattice potential has a profound effect on the Dirac cone. The dispersion of the first band above charge neutrality [red line in Fig. 2(b)] becomes nearly flat at the \mathbf{K} and \mathbf{K}' points of the moiré Brillouin zone due to nearby VHSs. Specifically, near \mathbf{K} and \mathbf{K}' , symmetry constrains the Taylor expansion of the dispersion to the form $\epsilon_{\pm}(\mathbf{k}) = \alpha k^2 \pm \eta(k_x^3 - 3k_x k_y^2)$, where \pm refers to the two valleys. This yields three VHSs near \mathbf{K} and \mathbf{K}' that map into each other under C_{3z} and provide the large DOS shown in Fig. 2(c). In addition, there is a local maximum (minimum) for $\alpha < 0$ (> 0) at $\mathbf{k} = 0$. At a critical value of $w/(v_FL)$ where $\alpha = 0$, the three nearby VHSs merge to form higher-order VHSs exactly at \mathbf{K} and \mathbf{K}' with a power-law diverging density of states [48–51], as found in Ref. [20]. Our results do not require fine tuning to the critical value of $w/(v_FL)$. Instead, we focus on the vicinity of the VHSs that produce a sharp peak in the density of states [highlighted by the horizontal line in Fig. 2(b)].

We estimate the realistic value of the Coulomb interaction U on the superlattice scale as follows: taking $L \sim 20\text{nm}$ and the dielectric constant of the environment to be $\epsilon \sim 5$, we estimate $U \sim e^2/4\pi\epsilon_0\epsilon L \sim 15\text{meV}$. Screening by surface electrons reduces the interaction: within the random phase approximation, $U_*(\mathbf{q}) = U(\mathbf{q})/[1 -$

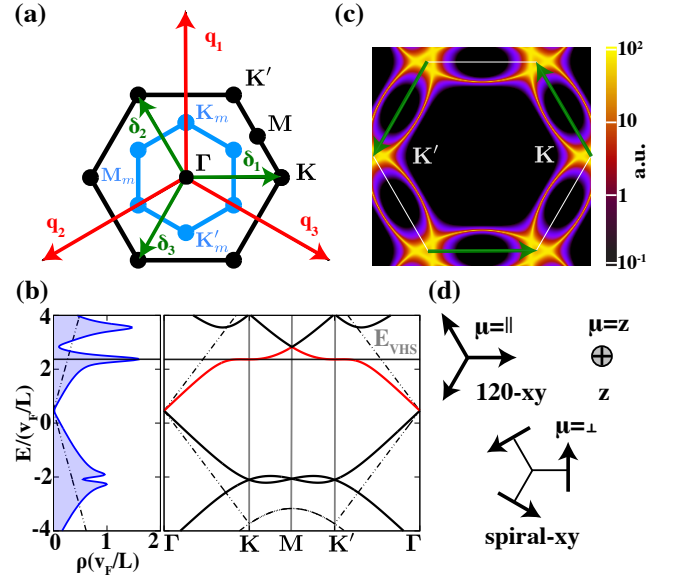


Figure 2. **Superlattice Brillouin zone, electronic properties of surface states and magnetic ordering basis.** (a) Black and cyan lines show the superlattice and magnetic Brillouin zones, respectively. The red and green arrows represent the wave vectors of the superlattice potential, \mathbf{q}_j , and the nesting vectors, $\boldsymbol{\delta}_j$, respectively. (b) Density of states and electronic dispersion for $w/(v_FL) \simeq 1.54$ ($L = 20\text{nm}$, $w = 20\text{meV}$). Dashed lines show the density of states and the band structure of the TI Dirac cone folded into the superlattice Brillouin zone and shifted to the charge neutrality point of the superlattice surface states. (c) Momentum resolved spectral function displaying the Fermi surface at the energy of the VHS with $w/(v_FL) \simeq 1.54$. (d) Decomposition of the order parameter into $\mathbf{v}_{\mu j}$.

$U(\mathbf{q})\Pi_0(\mathbf{q})]$, where $U(\mathbf{q}) = e^2/(4\pi\epsilon_0\epsilon q)$ and $\Pi_0(\mathbf{q})$ is the static density-density response. Scattering processes with momentum transfer $\mathbf{q} = \mathbf{K}' - \mathbf{K}$ connecting regions with large densities of states [Fig. 2(c)] are weakly affected by screening effects because electrons at \mathbf{K} and \mathbf{K}' occupy orthogonal Bloch states. As a result we find a finite density-density response $\Pi_0(\mathbf{K}' - \mathbf{K})$ and a weak renormalization of the Coulomb interaction U as detailed in the SM [52]. To describe the magnetic instability with momentum $\mathbf{K}' - \mathbf{K}$ we focus on the short-range Hubbard interaction:

$$\hat{H}_{\text{int}} = U \int d^2\mathbf{r} \hat{\Psi}_{\uparrow}^\dagger(\mathbf{r}) \hat{\Psi}_{\downarrow}^\dagger(\mathbf{r}) \hat{\Psi}_{\downarrow}(\mathbf{r}) \hat{\Psi}_{\uparrow}(\mathbf{r}); \quad U > 0, \quad (2)$$

where $\hat{\Psi}_{\uparrow,\downarrow}(\mathbf{r})$ is the electron annihilation operator, $\hat{\Psi}_{\sigma}(\mathbf{r}) = \sum_{\mathbf{k}, \mathbf{G}} e^{i(\mathbf{k}-\mathbf{G})\mathbf{r}} \hat{c}_{\mathbf{k}, \mathbf{G}, \sigma} / \sqrt{A}$ with A area of the sample, \mathbf{k} and \mathbf{G} label the Bloch momentum and reciprocal lattice vector of the moiré Brillouin zone, respectively, and $\hat{c}_{\mathbf{k}, \mathbf{G}, \sigma}^\dagger$ creates an electron at $\mathbf{k} - \mathbf{G}$ with spin σ . Notice that Ref. [20] considered an attractive interaction ($U < 0$) mediated by phonons and found the VHS enhanced the superconducting critical temperature.

The interaction term \hat{H}_{int} drives an instability towards

density wave ordering, modulated by the nesting vectors, $\delta_j = C_{3z}^{j-1}(\mathbf{K}' - \mathbf{K})$, which connect the \mathbf{K} and \mathbf{K}' regions where the DOS diverges at the VHS. The nesting vectors are indicated by green vectors in Fig. 2(a),(c) and define a magnetic Brillouin zone [solid cyan line in Fig. 2(a)] three times smaller than the original one. Spin-momentum locking is expected to drive the formation of an exotic spin-density wave (SDW) [40] spontaneously breaking time reversal symmetry on the TI surface. To study the SDW, we decompose the order parameters for each modulation δ_j [5] into an in-plane direction parallel to the nesting vector, $\mathbf{v}_{\parallel j} = \mathbf{e}_j \equiv \delta_j/|\delta_j|$; an in-plane direction perpendicular to the nesting vector, $\mathbf{v}_{\perp j} = -i(\mathbf{z} \times \mathbf{e}_j)$; and an out-of-plane part, $\mathbf{v}_{zj} = -i\mathbf{z}$. Correspondingly, for each wave vector δ_j , the SDW operator can be decomposed into Fourier components as $\hat{S}_{\mu j} = \sum_{\mathbf{k}} \sum_{\mathbf{G}} \hat{c}_{\mathbf{k}+\delta_j, \mathbf{G}, \sigma}^\dagger \mathbf{v}_{\mu j} \cdot \boldsymbol{\sigma}_{\sigma\sigma'} \hat{c}_{\mathbf{k}, \mathbf{G}, \sigma'}$ which represents the three types of magnetic order illustrated in Fig. 2(d).

Ginzburg-Landau mean field theory.—We study the magnetic order by deriving a Ginzburg-Landau theory. We assume a homogenous electron density n and a spatially-modulated magnetization $\mathbf{m}(\mathbf{r}) = \sum_{j=1}^3 (\mathbf{m}_{\delta_j} e^{i\delta_j \mathbf{r}} + \mathbf{m}_{-\delta_j} e^{-i\delta_j \mathbf{r}})$ where \mathbf{m}_{δ_j} is the Fourier amplitude associated to the modulation δ_j . Since $\mathbf{m}(\mathbf{r})$ is real, $\mathbf{m}_{\delta_j} = \mathbf{m}_{-\delta_j}^* \equiv \mathbf{m}_j$. We expand $\mathbf{m}_j = \sum_{\mu} s_{\mu j} \mathbf{v}_{\mu j}$ where $\mathbf{v}_{\mu j}$ are the normal modes in Fig. 2(d) and the order parameter $s_{\mu j} = \langle \hat{S}_{\mu j} \rangle / A$ is the average value of $\hat{S}_{\mu j}$. Employing the Hubbard-Stratonovich transformation [53–55] (details in the SM [52]) yields the free energy:

$$F = \frac{A}{2} \left(\sum_{\mu j} |s_{\mu j}|^2 - \frac{n^2}{2} \right) + \sum_{m=1}^{\infty} \text{Tr} \left[\frac{(-G_0 X)^m}{mU} \right], \quad (3)$$

where $G_0 = (-\partial_\tau - H_0 + \mu)^{-1}$ is the non-interacting single-particle Green's function, τ is imaginary time, and $X = U\mathbf{m}(\mathbf{r}) \cdot \boldsymbol{\sigma} / 2 - Un/2$ describes the interaction between the order parameter and the electrons.

The ground state magnetic order is determined by solving the saddle-point equations of the free energy (3), $\delta F / \delta n = 0$ and $\delta F / \delta s_{\mu j}^* = 0$. We solve these equations numerically, as detailed in the SM [52]. We find that in the range of filling between $n \sim 0.61$ and $n \sim 0.8$ the minimum of the free energy (3) develops a SDW magnetic ordering. The blue data in Fig. 3(a) shows the magnitude of the total magnetization density, $|M| = \sqrt{\sum_{\mu j} |s_{\mu j}|^2}$, as a function of the filling per unit cell of the superlattice.

In real space, the magnetic order $\mathbf{m}(\mathbf{r})$ obtained from the saddle-point solution forms a Néel-type meron lattice [25] with two merons in each unit cell, as shown in Fig. 3(b). The merons are well-defined because the magnetic moment is forced to be in-plane along mirror-invariant lines. Each meron can be characterized by the Pontryagin density $\Phi(\mathbf{r}) = \hat{\mathbf{m}}(\mathbf{r}) \cdot [\partial_x \hat{\mathbf{m}}(\mathbf{r}) \times \partial_y \hat{\mathbf{m}}(\mathbf{r})] / 4\pi$

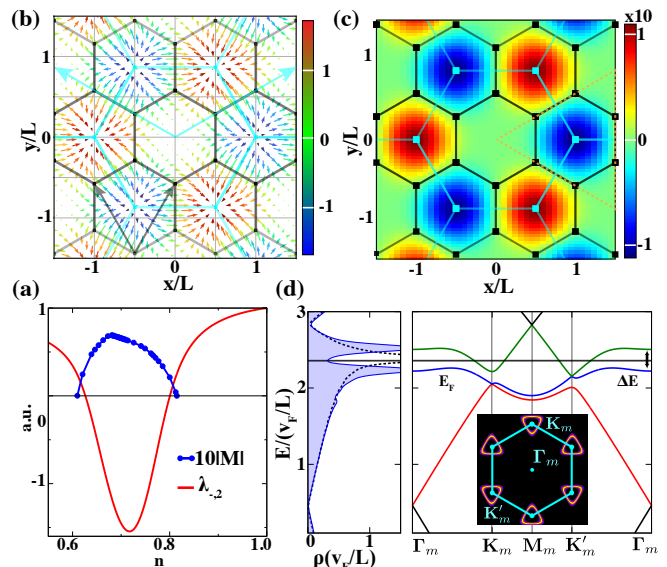


Figure 3. **Saddle-point solution, real-space magnetization and electronic structure in the meron lattice phase.** (a) Blue and red data show the absolute value of the magnetization obtained by solving the saddle-point equations and the lowest eigenvalue of $\mathcal{M}_{jl}^{\mu\nu}$, respectively. (b) Contour plot of magnetic order parameter in real space. The color refers to the out-of-plane component. (c) Winding number $\mathbf{m} \cdot (\partial_x \mathbf{m} \times \partial_y \mathbf{m}) / 4\pi$ in real-space. Black and cyan lines show the superlattice and magnetic unit cells, respectively, with primitive vectors $\mathbf{t}_{1/2} = L(\pm 1/2, \sqrt{3}/2)$ and $\mathbf{t}_{1/2}^* = \sqrt{3}L(\mp \sqrt{3}/2, 1/2)$. (d) Density of states and electronic dispersion of the meron lattice state. The dashed line shows the density of states in the presence of the superlattice in the normal phase. The horizontal line shows the Fermi energy E_F ; ΔE denotes the gap induced by the magnetic order at Γ_m . Inset shows the Fermi surface of the magnetic state. The bands are obtained from the Hartree-Fock solution at $w/(v_F/L) \simeq 1.54$, $2w = 40\text{meV}$, $U = 30\text{meV}$ and $T = 1.5\text{K}$.

shown in Fig. 3(c) where $\hat{\mathbf{m}}$ is a unit magnetization vector. We find $\int_S d^2\mathbf{r} \Phi(\mathbf{r}) = \pm 1/2$, where S is the triangular domain illustrated by the orange dashed line in Fig. 3(c). In the center of each unit cell is an intermediate region of destructive interference with vanishing magnetization. The magnetic order spontaneously breaks the translation symmetry of the potential, giving rise to a magnetic unit cell [cyan line in Fig. 3(b)] three times larger than the original one [black solid line in Fig. 3(b)].

We treat the effect of the magnetization on the electronic spectrum at the mean-field Hartree-Fock level by replacing $H_0(\mathbf{r})$ in Eq. (1) with

$$H_{\text{HF}}(\mathbf{r}) = H_0(\mathbf{r}) - U\mathbf{m}(\mathbf{r}) \cdot \boldsymbol{\sigma} / 2. \quad (4)$$

Despite breaking time-reversal symmetry, the resulting electronic spectrum remains gapless because the magnetic order preserves $C_{2z}T$ symmetry. The dispersion is plotted in the right panel of Fig. 3(d) in the magnetic Brillouin zone: the original red band in Fig. 2(b) is decomposed into three different bands given by the red,

blue and green lines in Fig. 3(d). The Dirac cones at \mathbf{K}_m between the red and blue bands and at \mathbf{K}'_m between the blue and the green ones are protected by $C_{2z}T$. Thus, they persist for arbitrary value of the interaction and give rise to a gapless electronic spectrum whose Fermi surface is shown in the inset of Fig. 3(d).

Although the order parameter $\mathbf{m}(\mathbf{r})$ does not open a full gap, it significantly reduces the density of states at the Fermi level (horizontal black dashed line in Fig. 3(d)) by opening a gap between the blue and green bands at Γ of order $\Delta E \propto U|M|$. The gap splits the peak in the DOS resulting from the VHS into two peaks above and below, as shown in the left panel of Fig. 3(d). The significant decrease in the kinetic energy from splitting the large peak in the DOS makes the magnetic state energetically favorable with respect to the normal one.

Phase diagram.—The instability of the Dirac cone surface state is determined by expanding the free energy for small values of the order parameter $s_{\mu j}$. As time-reversal symmetry acts on the order parameter by $T : s_{\mu j} \rightarrow -s_{\mu j}^*$, only even powers of $s_{\mu j}$ are allowed in the free energy (3), so that to second order in $s_{\mu j}$ at fixed density n , $F_{(2)} = \sum_{\mu\nu} \sum_{jl=1}^3 s_{\mu j}^* \mathcal{M}_{jl}^{\mu\nu} s_{\nu l} / 2$, where

$$\mathcal{M}_{jl}^{\mu\nu} = \delta_{\mu\nu} \delta_{jl} - U \chi_{jl}^{\mu\nu} / 2, \quad (5)$$

and $\chi_{jl}^{\mu\nu} \equiv \int_0^\beta d\tau \langle \hat{S}_{\mu j}^\dagger(\tau) \hat{S}_{\nu l}(0) \rangle / A$ is the thermodynamic spin susceptibility with τ imaginary time and β inverse temperature. Eq. (5) contains both diagonal terms ($j = l$), which come from momentum-conserving electron-hole scattering processes in the first superlattice Brillouin zone, and off-diagonal terms ($j \neq l$) from Umklapp processes where the electron-hole excitation is scattered outside the first Brillouin zone, transferring momentum $\delta_j - \delta_l \in \mathbf{G}$.

An instability exists when one of the eigenvalues of the matrix $\mathcal{M}_{jl}^{\mu\nu}$ becomes negative, which comprises a generalization of the Stoner criterion for ferromagnetism in metals [56]. The corresponding eigenvector indicates the magnetic configuration of the instability. The eigenvectors are classified by how they transform under symmetry. Since the saddle-point solution is C_{3z} -symmetric, we consider a C_{3z} -invariant eigenvector of $\mathcal{M}_{jl}^{\mu\nu}$, which implies the magnetization takes the form $s_{\mu j} = MU_\mu / \sqrt{3}$. It follows that

$$F_{(2)} = \frac{|M|^2}{2} \begin{pmatrix} U_{\parallel} \\ U_{\perp} \\ U_z \end{pmatrix}^\dagger \begin{pmatrix} L_{\parallel\parallel} & 0 & L_{\parallel z} \\ 0 & L_{\perp\perp} & 0 \\ L_{\parallel z} & 0 & L_{zz} \end{pmatrix} \begin{pmatrix} U_{\parallel} \\ U_{\perp} \\ U_z \end{pmatrix}, \quad (6)$$

where the elements $L_{\mu\nu} = \sum_{jl} \mathcal{M}_{jl}^{\mu\nu} / 3$ are shown in Fig. 4(a) as a function of the density at $T = 1.5\text{K}$. The perpendicular (U_{\perp}) component of the magnetic order is decoupled from the other components (U_{\parallel}, U_z) because it is even under the mirror m_y , while the parallel and z -components are odd. (The symmetries are discussed

in detail in the SM [52].) From Eq. (6), the surface Dirac cone is unstable when either $\lambda_1 = L_{\perp\perp} < 0$, which corresponds to in-plane order purely in the “spiral-xy” channel and even under m_y , or when one of the eigenvalues $\lambda_{\pm,2} = (L_{\parallel\parallel} + L_{zz})/2 \pm \sqrt{(L_{\parallel\parallel} - L_{zz})^2/4 + L_{\parallel z}^2} < 0$, which corresponds to a generically non-coplanar SDW with “120-xy” and z components, and breaking m_y [see Fig. 2(d).]

By computing the spin-susceptibility, $\chi_{jl}^{\mu\nu}$, as detailed in the SM [52], we find that for a range of filling near 2/3 electron per unit cell, the dominant instability occurs in the channel corresponding to $\lambda_{-,2}$, as shown by where the red solid line in Fig. 3(a) goes negative, and in agreement with our saddle-point solution. This solution, which breaks m_y , is energetically favored over the in-plane spin solution that is even in m_y because it allows a gap to open at Γ_m in the magnetic BZ, indicated by ΔE in Fig. 3(d). This gap splits the peak in the DOS from the VHS into two peaks, as shown in Fig. 3(d), which decreases the kinetic energy and lowers the energy of system relative to the non-magnetic state. The other magnetic state, with eigenvalue $\lambda_{+,2}$, also breaks m_y , but is energetically unfavourable because it exhibits a clockwise magnetization winding inconsistent with the intrinsic SOC of the surface state in Eq. (1). We have also studied the C_{3z} -breaking magnetic orders. Since these orders do not hybridize the states at \mathbf{K} and \mathbf{K}' , they do not split the peak in the DOS and do not lead to any magnetic instability. The symmetry and energetics of the magnetic orders are elaborated on in the SM [52].

The critical temperature and interaction strength occur at precisely the point where one of the eigenvalues of $\mathcal{M}_{jl}^{\mu\nu}$ changes sign. Fig. 4(b) shows the critical temperature for a range of fillings around the VHS at $U = 30\text{meV}$. The magnetic dome peaks at $T_c \sim 7\text{K}$ near an optimal value of $w/(v_F/L) \simeq 1.54$: surprisingly, the peak does not coincide with the higher-order VHS [20] at $w/(v_F/L) \simeq 1.36$. Fig. 4(c) shows the evolution of the energy and the number of electrons per superlattice unit cell where the VHS occurs as a function of $w/(v_F/L)$. The maximum critical temperature for the magnetic transition takes place around $n \sim 2/3$ filling of the superlattice unit cell, denoted as the horizontal green line in the inset of Fig. 4(c).

Fig. 4(d) shows the critical interaction U_c necessary to induce the magnetic instability as a function of the filling n for different values of the temperature T . Lowering the temperature reduces the magnetic transition to arbitrarily weak repulsive interactions. Our estimate of $U \sim 15\text{meV}$ [below Eq. (2)] is well above the critical interaction strength required for $T \leq 1.5\text{K}$ as shown by the black dashed line in Fig. 4(d). In contrast, in the absence of the superlattice potential, spontaneous magnetization of the surface state [5, 12–18] in the Bi_2Se_3 family requires a much larger critical value of the Coulomb in-

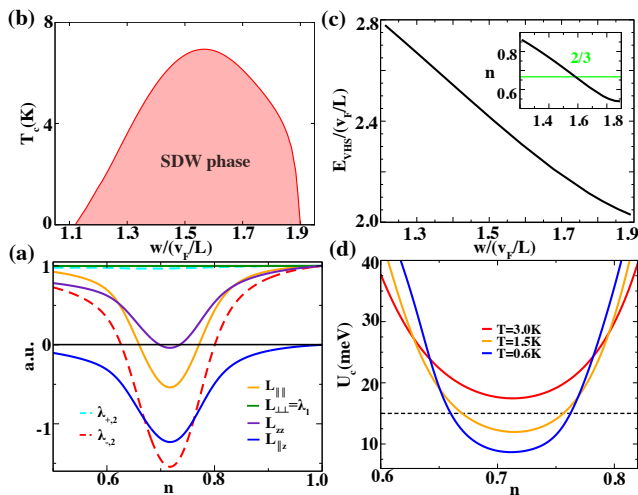


Figure 4. **Magnetic instability and critical temperature and interaction.** (a) Solid lines show the components of the second order free energy $L_{\mu\nu}$. Red and cyan dashed lines illustrate the eigenvalues $\lambda_{-,2}$ and $\lambda_{+,2}$, respectively, while $\lambda_1 = L_{\perp\perp}$ is the solid green line. The calculations were performed at $T = 1.5$ K, $U = 30$ meV and $w/(v_F/L) \simeq 1.54$. (b) Critical temperature for the magnetic transition as a function of $w/(v_F/L)$ for $U = 30$ meV. For a given $w/(v_F/L)$, the filling n is set so that the Fermi level is at the energy of the VHS. (c) Evolution of the energy of the VHS singularity as a function of $w/(v_F/L)$. Inset shows the electron filling per superlattice unit cell at the VHS versus $w/(v_F/L)$. (d) Critical interaction U_c for the magnetic instability as a function of the filling n at several temperatures, fixing $2w = 40$ meV and $w/(v_F/L) \simeq 1.54$. Lowering the temperature reduces the critical interaction down to an arbitrarily weak interaction. The black dashed line indicates our rough estimate of $U \sim 15$ meV.

teraction, on the order of 2 eV [13, 14, 18]. Thus, the superlattice potential makes this magnetic instability experimentally accessible. We expect our results are robust to weak disorder, which will reduce the transition temperature [57, 58] without eliminating the magnetic state.

Hexagonal warping.— Beyond the linear momentum dependence of the Dirac cone in Eq. (1) the dispersion develops a hexagonal warping term $H_w(\mathbf{k}) = \lambda(k_x^3 - 3k_x k_y^2)\sigma_z$ [5]. Despite being small in $(4\pi)^2\lambda/3v_FL^2$ this correction gives rise to a series of interesting effects that are experimentally relevant. The hexagonal warping breaks m_y and $C_{2z}T$ symmetries, which allows the perpendicular component of spin, U_\perp , to mix with the parallel and z components, U_\parallel and U_z . As a result, the magnetization develops a finite U_\perp component. The m_x and C_{3z} symmetries continue to protect the Dirac cones at \mathbf{K}_m and \mathbf{K}'_m in Fig. 3(d), so the surface remains gapless. While the average magnetic moment in the unit cell continues to vanish, $\int d^2\mathbf{r} m_i = 0$, the explicitly broken m_y symmetry gives rise to a finite out-of-plane toroidal moment $\mathcal{T}_z = \int d^2\mathbf{r} \varepsilon_{ij} r_i m_j / 2$ where ε_{ij} is the Levi-Civita symbol and a sum over repeated indices is assumed. A non-zero \mathcal{T}_z [59–61] typically manifests in the magneto-

electric susceptibility $\alpha_{xy} = -\alpha_{yx}$ [62, 63] implying an in-plane uniform magnetization perpendicular to the applied electric field $m_i = \alpha_{ij} E_j$. Strain [64–66] and lattice relaxation effects may also favour the broken mirror symmetry, further enhancing \mathcal{T}_z .

Experimental detection.— The meron lattice phase can be measured by directly imaging the magnetization pattern in real space through Lorentz transmission electron microscopy [26, 67] and nitrogen vacancy magnetometry [68] or in reciprocal space via X-ray diffraction [22, 69–74]. The spontaneous magnetization can also be measured through magneto-optical measurements such as the magneto-optical Kerr effect (MOKE) [75, 76] and reflective magnetic circular dichroism (RMDC) [77]. In addition, the magnetoelectric susceptibility α_{xy} can be observed either by measuring an in-plane magnetization in response to an electric field, or a current resulting from an in-plane magnetic field; these are related through Onsager relations. The reduced density of states resulting from the magnetic order, as shown in Fig. 3(d), should result in a drastic variation of the electronic compressibility across the transition. Finally, we also expect that the response to an applied magnetic field [78–84] gives rise to distinctive signatures of the meron state.

Discussion.— We have shown that a superlattice potential applied to the surface of a TI provides a new route to spontaneously breaking time reversal symmetry on the TI surface. The magnetic order realizes a novel meron lattice exhibiting pairs of merons with opposite topological charge in the unit cell, shown in Fig. 3(b) and (c). The periodicity of the meron lattice is determined by the period of the potential; consequently, the meron lattice periodicity is completely tunable. Although the magnetic order breaks time-reversal, it preserves $C_{2z}T$ and thus does not open a gap on the TI surface. This instability is much stronger than that induced by hexagonal warping because it is driven by a VHS [20] that results from the superlattice potential. Thus, we predict that the magnetic order can be observed at realistic temperature and interaction strength, as summarized in Fig. 4, overcoming the obstacles of previous work as a consequence of the tunable superlattice potential.

This finding has far-reaching consequences, as this unconventional magnetic state will have implications both on the experimental and on the theoretical level. First, the topological spin texture realizes an electromagnetic field on the scale of the superlattice that can be employed by proximity effects to modify band structure and topological properties of electronic systems [33, 37, 85–89]. Second, the broken mirror symmetry that results from hexagonal warping of the Fermi surface implies that the meron lattice hosts a magnetoelectric response with potential application to spintronics [88–93]. This unconventional effect can be strongly enhanced by strain [64–66] and lattice relaxation [94]. A quantitative estimation of the magnetoelectric response in the system will require

extensive numerical studies taking into account lattice relaxation effects on the surface of the TI. Finally, we envision a superconducting transition mediated by the spin-fluctuations of the underlying topological magnetic ordering. The mechanism is an alternative to the phonon-mediated pairing pointed out in Ref. [20]. A detailed analysis will stimulate future theoretical and experimental investigations.

Acknowledgements. — We have benefited from discussions with Yang-Zhi Chou, M. Michael Denner, Shiang Fang, Jiawei Zang, Andrew J. Millis, Zhentao Wang, Tiancheng Song, and Justin Wilson. We are grateful to L. Reading-Ikkanda for creating the figure of the experimental setup and the sketch of the magnetic state. We also acknowledge the support of the Flatiron Institute, a division of the Simons Foundation. This work was partially supported by the Air Force Office of Scientific Research under Grant No. FA9550-20-1-0260 (J.C.) and Grant No. FA9550-20-1-0136 (J.H.P.) and the Alfred P. Sloan Foundation through a Sloan Research Fellowship (J.H.P.). J.H.P. and J.C. acknowledge hospitality of the Aspen Center for Physics, where some of this work was developed and which is supported by National Science Foundation grant PHY1607611.

-
- [1] L. Fu, C. L. Kane, and E. J. Mele, Topological insulators in three dimensions, *Phys. Rev. Lett.* **98**, 106803 (2007).
- [2] J. E. Moore and L. Balents, Topological invariants of time-reversal-invariant band structures, *Phys. Rev. B* **75**, 121306 (2007).
- [3] R. Roy, Topological phases and the quantum spin hall effect in three dimensions, *Phys. Rev. B* **79**, 195322 (2009).
- [4] M. König, S. Wiedmann, C. Brüne, A. Roth, H. Buhmann, L. W. Molenkamp, X.-L. Qi, and S.-C. Zhang, Quantum spin hall insulator state in hgte quantum wells, *Science* **318**, 766 (2007), <https://www.science.org/doi/pdf/10.1126/science.1148047>.
- [5] L. Fu, Hexagonal warping effects in the surface states of the topological insulator Bi_2Te_3 , *Phys. Rev. Lett.* **103**, 266801 (2009).
- [6] D. Hsieh, D. Qian, L. Wray, Y. Xia, Y. S. Hor, R. J. Cava, and M. Z. Hasan, A topological dirac insulator in a quantum spin hall phase (experimental realization of a 3d topological insulator) (2009), [arXiv:0910.2420 \[cond-mat.mes-hall\]](https://arxiv.org/abs/0910.2420).
- [7] D. Hsieh, Y. Y. Xia, D. Qian, L. A. Wray, J. H. Dil, F. Meier, J. Osterwalder, L. Patthey, J. G. Checkelsky, N. P. Ong, A. V. Fedorov, H. I. Lin, A. Bansil, D. Grauer, Y. S. Hor, R. J. Cava, and M. Z. Hasan, A tunable topological insulator in the spin helical dirac transport regime, *Nature* **460**, 1101 (2009).
- [8] Y. L. Chen, J. G. Analytis, J.-H. Chu, Z. K. Liu, S.-K. Mo, X. L. Qi, H. J. Zhang, D. H. Lu, X. Dai, Z. Fang, S. C. Zhang, I. R. Fisher, Z. Hussain, and Z.-X. Shen, Experimental realization of a three-dimensional topological insulator, Bi_2Te_3 , *Science* **325**, 178 (2009), <https://www.science.org/doi/pdf/10.1126/science.1173034>.
- [9] Y. Xia, D. Qian, D. Hsieh, L. A. Wray, A. Pal, H. Lin, A. Bansil, D. Grauer, Y. S. Hor, R. J. Cava, and M. Z. Hasan, Observation of a large-gap topological-insulator class with a single dirac cone on the surface, *Nature Physics* **5**, 398 (2009).
- [10] C. Brüne, C. X. Liu, E. G. Novik, E. M. Hankiewicz, H. Buhmann, Y. L. Chen, X. L. Qi, Z. X. Shen, S. C. Zhang, and L. W. Molenkamp, Quantum hall effect from the topological surface states of strained bulk hgte, *Phys. Rev. Lett.* **106**, 126803 (2011).
- [11] S. Souma, K. Kosaka, T. Sato, M. Komatsu, A. Takayama, T. Takahashi, M. Kriener, K. Segawa, and Y. Ando, Direct measurement of the out-of-plane spin texture in the dirac-cone surface state of a topological insulator, *Phys. Rev. Lett.* **106**, 216803 (2011).
- [12] J.-H. Jiang and S. Wu, Spin susceptibility and helical magnetic order at the edges/surfaces of topological insulators due to fermi surface nesting, *Phys. Rev. B* **83**, 205124 (2011).
- [13] Y. Baum and A. Stern, Magnetic instability on the surface of topological insulators, *Phys. Rev. B* **85**, 121105 (2012).
- [14] Y. Baum and A. Stern, Density-waves instability and a skyrmion lattice on the surface of strong topological insulators, *Physical Review B* **86**, 10.1103/physrevb.86.195116 (2012).
- [15] D. J. J. Marchand and M. Franz, Lattice model for the surface states of a topological insulator with applications to magnetic and exciton instabilities, *Phys. Rev. B* **86**, 155146 (2012).
- [16] M. J. Schmidt, Strong correlations at topological insulator surfaces and the breakdown of the bulk-boundary correspondence, *Phys. Rev. B* **86**, 161110 (2012).
- [17] M. Sitte, A. Rosch, and L. Fritz, Interaction effects on almost flat surface bands in topological insulators, *Phys. Rev. B* **88**, 205107 (2013).
- [18] D. Mendler, P. Kotetes, and G. Schön, Magnetic order on a topological insulator surface with warping and proximity-induced superconductivity, *Phys. Rev. B* **91**, 155405 (2015).
- [19] J. Cano, S. Fang, J. H. Pixley, and J. H. Wilson, Moiré superlattice on the surface of a topological insulator, *Phys. Rev. B* **103**, 155157 (2021).
- [20] T. Wang, N. F. Q. Yuan, and L. Fu, Moiré surface states and enhanced superconductivity in topological insulators, *Phys. Rev. X* **11**, 021024 (2021).
- [21] N. Gao, S. G. Je, M. Y. Im, J. W. Choi, M. Yang, Q. Li, T. Y. Wang, S. Lee, H. S. Han, K. S. Lee, W. Chao, C. Hwang, J. Li, and Z. Q. Qiu, Creation and annihilation of topological meron pairs in in-plane magnetized films, *Nature Communications* **10**, 10.1038/s41467-019-13642-z (2019).
- [22] S. Muhlbauer, B. Binz, F. Jonietz, C. Pfleiderer, A. Rosch, A. Neubauer, R. Georgii, and P. Boni, Skyrmion lattice in a chiral magnet, *Science* **323**, 915 (2009).
- [23] C. Pappas, E. Lelièvre-Berna, P. Falus, P. M. Bentley, E. Moskvina, S. Grigoriev, P. Fouquet, and B. Farago, Chiral paramagnetic skyrmion-like phase in MnSi, *Phys. Rev. Lett.* **102**, 197202 (2009).
- [24] A. Neubauer, C. Pfleiderer, B. Binz, A. Rosch, R. Ritz, P. G. Niklowitz, and P. Böni, Topological hall effect in the a phase of MnSi, *Phys. Rev. Lett.* **102**, 186602 (2009).
- [25] N. Nagaosa and Y. Tokura, Topological properties and

- dynamics of magnetic skyrmions, *Nature nanotechnology* **8**, 899 (2013).
- [26] S. Heinze, K. von Bergmann, M. Menzel, J. Brede, A. Kubetzka, R. Wiesendanger, G. Bihlmayer, and S. Blügel, Spontaneous atomic-scale magnetic skyrmion lattice in two dimensions, *Nat Phys* **7**, 713 (2011).
- [27] N. Romming, C. Hanneken, M. Menzel, J. E. Bickel, B. Wolter, K. von Bergmann, A. Kubetzka, and R. Wiesendanger, Writing and deleting single magnetic skyrmions, *Science* **341**, 636 (2013), <https://www.science.org/doi/pdf/10.1126/science.1240573>.
- [28] I. Gross, W. Akhtar, A. Hrabec, J. Sampaio, L. J. Martínez, S. Chouaieb, B. J. Shields, P. Maletinsky, A. Thiaville, S. Rohart, and V. Jacques, Skyrmion morphology in ultrathin magnetic films, *Phys. Rev. Materials* **2**, 024406 (2018).
- [29] S. Seki, X. Z. Yu, S. Ishiwata, and Y. Tokura, Observation of skyrmions in a multiferroic material, *Science* **336**, 198 (2012), <https://www.science.org/doi/pdf/10.1126/science.1214143>.
- [30] X. Yu, M. Mostovoy, Y. Tokunaga, W. Zhang, K. Kimoto, Y. Matsui, Y. Kaneko, N. Nagaosa, and Y. Tokura, Magnetic stripes and skyrmions with helicity reversals, *Proceedings of the National Academy of Sciences* **109**, 8856–8860 (2012).
- [31] X. Z. Yu, W. Koshibae, Y. Tokunaga, K. Shibata, Y. Taguchi, N. Nagaosa, and Y. Tokura, Transformation between meron and skyrmion topological spin textures in a chiral magnet, *Nature* **564**, 95 (2018).
- [32] S. Gao, H. D. Rosales, F. A. G. Albarracín, V. Tsurkan, G. Kaur, T. Fennell, P. Steffens, M. Boehm, P. Čermák, A. Schneidewind, E. Ressouche, D. C. Cabra, C. Rüegg, and O. Zaharko, Fractional antiferromagnetic skyrmion lattice induced by anisotropic couplings, *Nature* **586**, 37 (2020).
- [33] S. Divic, H. Ling, T. Pereg-Barnea, and A. Paramekanti, Magnetic skyrmion crystal at a topological insulator surface (2021), [arXiv:2103.15841 \[cond-mat.mes-hall\]](https://arxiv.org/abs/2103.15841).
- [34] K. Nomura and N. Nagaosa, Electric charging of magnetic textures on the surface of a topological insulator, *Phys. Rev. B* **82**, 161401 (2010).
- [35] H. M. Hurst, D. K. Efimkin, J. Zang, and V. Galitski, Charged skyrmions on the surface of a topological insulator, *Phys. Rev. B* **91**, 060401 (2015).
- [36] K. L. Tiwari, J. Lavoie, T. Pereg-Barnea, and W. A. Coish, Tunable skyrmion-skyrmion binding on the surface of a topological insulator, *Phys. Rev. B* **100**, 125414 (2019).
- [37] N. Paul and L. Fu, Topological magnetic textures in magnetic topological insulators, *Physical Review Research* **3**, 10.1103/physrevresearch.3.033173 (2021).
- [38] C. Forsythe, X. Zhou, K. Watanabe, T. Taniguchi, A. Papaty, P. Moon, M. Koshino, P. Kim, and C. R. Dean, Band structure engineering of 2d materials using patterned dielectric superlattices, *Nature Nanotechnology* **13**, 566–571 (2018).
- [39] Y. Li, S. Dietrich, C. Forsythe, T. Taniguchi, K. Watanabe, P. Moon, and C. R. Dean, Anisotropic band flattening in graphene with one-dimensional superlattices, *Nature Nanotechnology* **16**, 525 (2021).
- [40] Y.-Z. Chou, J. Cano, and J. H. Pixley, Band manipulation and spin texture in interacting moiré helical edges, *Physical Review B* **104**, 10.1103/physrevb.104.120113 (2021).
- [41] Z. Liu, H. Wang, and J. Wang, Magnetic moiré surface states and flat chern band in topological insulators (2021), [arXiv:2106.01630 \[cond-mat.mes-hall\]](https://arxiv.org/abs/2106.01630).
- [42] L.-k. Shi, J. Ma, and J. C. Song, Gate-tunable flat bands in van der waals patterned dielectric superlattices, *2D Materials* **7**, 015028 (2019).
- [43] J. Zhang, C. Triola, and E. Rossi, Proximity effect in graphene–topological-insulator heterostructures, *Phys. Rev. Lett.* **112**, 096802 (2014).
- [44] K. Schouteden, Z. Li, T. Chen, F. Song, B. Partoens, C. Van Haesendonck, and K. Park, Moiré superlattices at the topological insulator Bi_2Te_3 , *Scientific Reports* **6**, 20278 (2016).
- [45] A. Vargas, F. Liu, C. Lane, D. Rubin, I. Bilgin, Z. Hennighausen, M. DeCapua, A. Bansil, and S. Kar, Tunable and laser-reconfigurable 2d heterocrystals obtained by epitaxial stacking of crystallographically incommensurate Bi_2Se_3 and MoS_2 atomic layers, *Science Advances* **3**, e1601741 (2017), <https://www.science.org/doi/pdf/10.1126/sciadv.1601741>.
- [46] Z. Hennighausen, C. Lane, I. G. Buda, V. K. Mathur, A. Bansil, and S. Kar, Evidence of a purely electronic two-dimensional lattice at the interface of $\text{TMD}/\text{Bi}_2\text{Se}_3$ heterostructures, *Nanoscale* **11**, 10.1039/c9nr04412d (2019).
- [47] A. Dunbrack and J. Cano, Magic angle conditions for twisted 3d topological insulators (2021), [arXiv:2112.11464 \[cond-mat.str-el\]](https://arxiv.org/abs/2112.11464).
- [48] N. F. Q. Yuan and L. Fu, Classification of critical points in energy bands based on topology, scaling, and symmetry, *Phys. Rev. B* **101**, 125120 (2020).
- [49] N. F. Q. Yuan, H. Isobe, and L. Fu, Magic of high-order van hove singularity, *Nature Communications* **10**, 10.1038/s41467-019-13670-9 (2019).
- [50] A. Chandrasekaran, A. Shtyk, J. J. Betouras, and C. Chamon, Catastrophe theory classification of fermi surface topological transitions in two dimensions, *Phys. Rev. Research* **2**, 013355 (2020).
- [51] D. Guerci, P. Simon, and C. Mora, Higher-order van hove singularity in magic-angle twisted trilayer graphene (2021), [arXiv:2106.14911 \[cond-mat.mes-hall\]](https://arxiv.org/abs/2106.14911).
- [52] See Supplementary Material at url ... for details on the continuum model, the derivation of the Landau Ginzburg free energy, the solution of the saddle-point equations and the symmetries of the skyrmion lattice.
- [53] C. Mudry, *Lecture Notes on Field Theory in Condensed Matter Physics* (WORLD SCIENTIFIC, 2014) <https://www.worldscientific.com/doi/pdf/10.1142/8697>.
- [54] E. Fradkin, *Field Theories of Condensed Matter Physics*, 2nd ed. (Cambridge University Press, 2013).
- [55] A. Altland and B. D. Simons, *Condensed Matter Field Theory*, 2nd ed. (Cambridge University Press, 2010).
- [56] E. C. Stoner, Collective electron ferromagnetism, *Proceedings of the Royal Society of London. Series A. Mathematical and Physical Sciences* **165**, 372 (1938), <https://royalsocietypublishing.org/doi/pdf/10.1098/rspa.1938.0066>.
- [57] G. Litak, A. Martin, B. Györfy, J. Annett, and K. Wysokiński, Van hove singularity and d-wave pairing in disordered superconductors, *Physica C: Superconductivity* **309**, 257–262 (1998).
- [58] J. H. Wilson, Y. Fu, S. Das Sarma, and J. H. Pixley, Disorder in twisted bilayer graphene, *Physical Review Research* **2**, 10.1103/physrevresearch.2.023325 (2020).
- [59] K. Sawada and N. Nagaosa, Optical magnetoelectric ef-

- fect in multiferroic materials: Evidence for a lorentz force acting on a ray of light, *Phys. Rev. Lett.* **95**, 237402 (2005).
- [60] C. Ederer and N. A. Spaldin, Towards a microscopic theory of toroidal moments in bulk periodic crystals, *Phys. Rev. B* **76**, 214404 (2007).
- [61] S. Bhowal and N. A. Spaldin, Magnetoelectric classification of skyrmions (2022), [arXiv:2201.01667](https://arxiv.org/abs/2201.01667) [[cond-mat.mes-hall](https://arxiv.org/archive/cond)].
- [62] S. Zhong, J. E. Moore, and I. Souza, Gyrotropic magnetic effect and the magnetic moment on the fermi surface, *Physical Review Letters* **116**, [10.1103/physrevlett.116.077201](https://doi.org/10.1103/physrevlett.116.077201) (2016).
- [63] J. Ma and D. A. Pesin, Chiral magnetic effect and natural optical activity in metals with or without weyl points, *Phys. Rev. B* **92**, 235205 (2015).
- [64] Z. Bi, N. F. Q. Yuan, and L. Fu, Designing flat bands by strain, *Physical Review B* **100**, [10.1103/physrevb.100.035448](https://doi.org/10.1103/physrevb.100.035448) (2019).
- [65] L. Balents, General continuum model for twisted bilayer graphene and arbitrary smooth deformations, *SciPost Physics* **7**, [10.21468/scipostphys.7.4.048](https://doi.org/10.21468/scipostphys.7.4.048) (2019).
- [66] W.-Y. He, D. Goldhaber-Gordon, and K. T. Law, Giant orbital magnetoelectric effect and current-induced magnetization switching in twisted bilayer graphene, *Nature Communications* **11**, [10.1038/s41467-020-15473-9](https://doi.org/10.1038/s41467-020-15473-9) (2020).
- [67] X. Yu, Y. Onose, N. Kanazawa, J. Park, J. Han, Y. Matsui, N. Nagaosa, and Y. Tokura, Real-space observation of a two-dimensional skyrmion crystal, *Nature* **465**, 901 (2010).
- [68] Y. Dovzhenko, F. Casola, S. Schlotter, T. X. Zhou, F. Büttner, R. L. Walsworth, G. S. D. Beach, and A. Yacoby, Magnetostatic twists in room-temperature skyrmions explored by nitrogen-vacancy center spin texture reconstruction, *Nature Communications* **9**, [10.1038/s41467-018-05158-9](https://doi.org/10.1038/s41467-018-05158-9) (2018).
- [69] S. V. Grigoriev, V. A. Dyadkin, D. Menzel, J. Schoenes, Y. O. Chetverikov, A. I. Okorokov, H. Eckerlebe, and S. V. Maleyev, Magnetic structure of $\text{Fe}_{1-x}\text{Co}_x\text{Si}$ in a magnetic field studied via small-angle polarized neutron diffraction, *Phys. Rev. B* **76**, 224424 (2007).
- [70] S. Seki, J.-H. Kim, D. S. Inosov, R. Georgii, B. Keimer, S. Ishiwata, and Y. Tokura, Formation and rotation of skyrmion crystal in the chiral-lattice insulator Cu_2OSeO_3 , *Phys. Rev. B* **85**, 220406 (2012).
- [71] S. V. Grigoriev, D. Chernyshov, V. A. Dyadkin, V. Dmitriev, S. V. Maleyev, E. V. Moskvina, D. Menzel, J. Schoenes, and H. Eckerlebe, Crystal handedness and spin helix chirality in $\text{Fe}_{1-x}\text{Co}_x\text{Si}$, *Phys. Rev. Lett.* **102**, 037204 (2009).
- [72] H. Wilhelm, M. Baenitz, M. Schmidt, U. K. Rößler, A. A. Leonov, and A. N. Bogdanov, Precursor phenomena at the magnetic ordering of the cubic helimagnet FeGe , *Phys. Rev. Lett.* **107**, 127203 (2011).
- [73] M. Hirschberger, T. Nakajima, S. Gao, L. Peng, A. Kikkawa, T. Kurumaji, M. Kriener, Y. Yamasaki, H. Sagayama, H. Nakao, K. Ohishi, K. Kakurai, Y. Taguchi, X. Yu, T. Hisa Arima, and Y. Tokura, Skyrmion phase and competing magnetic orders on a breathing kagomé lattice, *Nature Communications* **10** (2019).
- [74] R. Brearton, L. Turnbull, J. Verezhak, G. Balakrishnan, P. Hatton, G. Laan, and T. Hesjedal, Deriving the skyrmion hall angle from skyrmion lattice dynamics, *Nature Communications* **12**, 2723 (2021).
- [75] B. Huang, G. Clark, E. Navarro-Moratalla, D. R. Klein, R. Cheng, K. L. Seyler, D. Zhong, E. Schmidgall, M. A. McGuire, D. H. Cobden, W. Yao, D. Xiao, P. Jarillo-Herrero, and X. Xu, Layer-dependent ferromagnetism in a van der waals crystal down to the monolayer limit, *Nature* **546**, 270–273 (2017).
- [76] J. Liu, A. Singh, B. Kuerbanjiang, C. H. W. Barnes, and T. Hesjedal, Kerr effect anomaly in magnetic topological insulator superlattices, *Nanotechnology* **31**, 434001 (2020).
- [77] T. Song, X. Cai, M. W.-Y. Tu, X. Zhang, B. Huang, N. P. Wilson, K. L. Seyler, L. Zhu, T. Taniguchi, K. Watanabe, M. A. McGuire, D. H. Cobden, D. Xiao, W. Yao, and X. Xu, Giant tunneling magnetoresistance in spin-filter van der waals heterostructures, *Science* **360**, 1214–1218 (2018).
- [78] J. Ye, Y. B. Kim, A. J. Millis, B. I. Shraiman, P. Majumdar, and Z. Tešanović, Berry phase theory of the anomalous hall effect: Application to colossal magnetoresistance manganites, *Phys. Rev. Lett.* **83**, 3737 (1999).
- [79] Y. Taguchi, Y. Oohara, H. Yoshizawa, N. Nagaosa, and Y. Tokura, Spin chirality, berry phase, and anomalous hall effect in a frustrated ferromagnet, *Science* **291**, 2573 (2001), <https://www.science.org/doi/pdf/10.1126/science.1058161>.
- [80] P. Bruno, V. K. Dugaev, and M. Taillefumier, Topological hall effect and berry phase in magnetic nanostructures, *Phys. Rev. Lett.* **93**, 096806 (2004).
- [81] M. Onoda, G. Tatara, and N. Nagaosa, Anomalous hall effect and skyrmion number in real and momentum spaces, *Journal of the Physical Society of Japan* **73**, 2624 (2004).
- [82] B. Binz and A. Vishwanath, Chirality induced anomalous-hall effect in helical spin crystals, *Physica B: Condensed Matter* **403**, 1336 (2008).
- [83] N. Nagaosa and Y. Tokura, Emergent electromagnetism in solids, *Physica Scripta* **T146**, 014020 (2012).
- [84] T. Schulz, R. Ritz, A. Bauer, M. Halder, M. Wagner, C. Franz, C. Pfleiderer, K. Everschor, M. Garst, and A. Rosch, Emergent electrodynamics of skyrmions in a chiral magnet, *Nature Physics* **8**, 301 (2012).
- [85] H. M. Hurst, D. K. Efimkin, J. Zang, and V. Galitski, Charged skyrmions on the surface of a topological insulator, *Phys. Rev. B* **91**, 060401 (2015).
- [86] K. Shimizu, S. Okumura, Y. Kato, and Y. Motome, Spin moiré engineering of topological magnetism and emergent electromagnetic fields, *Physical Review B* **103**, [10.1103/physrevb.103.184421](https://doi.org/10.1103/physrevb.103.184421) (2021).
- [87] Y. Guan, O. V. Yazyev, and A. Kruchkov, Unconventional flat chern bands and $2e$ charges in skyrmionic moiré superlattices (2021), [arXiv:2111.10410](https://arxiv.org/abs/2111.10410) [[cond-mat.str-el](https://arxiv.org/archive/cond)].
- [88] J. Wang, J. Zang, J. Cano, and A. J. Millis, Staggered Pseudo Magnetic Field in Twisted Transition Metal Dichalcogenides: Physical Origin and Experimental Consequences, *arXiv e-prints*, [arXiv:2110.14570](https://arxiv.org/abs/2110.14570) (2021), [arXiv:2110.14570](https://arxiv.org/abs/2110.14570) [[cond-mat.mes-hall](https://arxiv.org/archive/cond)].
- [89] J. Zang, J. Wang, J. Cano, and A. J. Millis, Hartree-fock study of the moiré hubbard model for twisted bilayer transition metal dichalcogenides, *Phys. Rev. B* **104**, 075150 (2021).
- [90] A. Fert, V. Cros, and J. Sampaio, Skyrmions on the track,

- Nature Nanotechnology* **8**, 152–156 (2013).
- [91] A. Fert, N. Reyren, and V. Cros, Magnetic skyrmions: advances in physics and potential applications, *Nature Reviews Materials* **2**, [10.1038/natrevmats.2017.31](https://doi.org/10.1038/natrevmats.2017.31) (2017).
- [92] X. Zhang, M. Ezawa, and Y. Zhou, Magnetic skyrmion logic gates: conversion, duplication and merging of skyrmions, *Scientific Reports* **5**, [10.1038/srep09400](https://doi.org/10.1038/srep09400) (2015).
- [93] X. Zhang, Y. Zhou, K. Mee Song, T.-E. Park, J. Xia, M. Ezawa, X. Liu, W. Zhao, G. Zhao, and S. Woo, Skyrmion-electronics: writing, deleting, reading and processing magnetic skyrmions toward spintronic applications, *Journal of Physics: Condensed Matter* **32**, 143001 (2020).
- [94] N. N. T. Nam and M. Koshino, Lattice relaxation and energy band modulation in twisted bilayer graphene, *Phys. Rev. B* **96**, 075311 (2017).

Supplementary Material for Designer Skyrmion Lattice on the Surface of a Topological Insulator

Daniele Guerci,¹ Jie Wang,¹ J. H. Pixley,^{2,1} and Jennifer Cano^{3,1}

¹Center for Computational Quantum Physics, Flatiron Institute, New York, New York 10010, USA

²Department of Physics and Astronomy, Center for Materials Theory,
Rutgers University, Piscataway, New Jersey 08854, USA

³Department of Physics and Astronomy, Stony Brook University, Stony Brook, New York 11974, USA

These supplementary materials contain the details of analytic calculations as well as additional numerical details supporting the results presented in the main text. Sec. I contains the details on the continuum Hamiltonian for a surface Dirac cone in the presence of a superlattice potential. In addition we also discuss the screening of the Coulomb interaction and detail the Hartree-Fock Hamiltonian H_{HF} . In Sec. II we explicitly detail the action of the symmetries of the model on the spin-density wave (SDW) operators. The Hubbard-Stratonovich transformation and details on the solution of the saddle-point equations are given in Sec. III. Sec. IV contains the Ginzburg-Landau theory, the group-theoretical symmetry classification of the different magnetic states. In Sec. V we detail the real-space properties of the skyrmion lattice and we discuss the magnetoelectric moment. Finally, in Sec. VI we provide a simple calculation that clarifies the origin on the unconventional magnetic state.

I. DETAILS OF THE MODEL HAMILTONIAN

Hamiltonian.— The Hamiltonian of the continuum model is:

$$H_0(\mathbf{r}) = v_F(k_x\sigma_y - k_y\sigma_x) + \sigma_0 w(\mathbf{r}), \quad (1)$$

where the moiré potential is given by,

$$w(\mathbf{r}) = 2w \sum_{j=1}^3 \cos(\mathbf{q}_j \cdot \mathbf{r}), \quad \mathbf{q}_j = \frac{4\pi}{\sqrt{3}L} \left(-\sin \frac{2\pi(j-1)}{3}, \cos \frac{2\pi(j-1)}{3} \right), \quad (2)$$

for $j = 1, 2, 3$. The length scale L is the period of the moiré potential. To be concrete, we set $v_F = 2.55\text{eV}\text{\AA}$, the value measured experimentally in Bi_2Te_3 [1, 2]. We project $H_0(\mathbf{r})$ on the plane wave basis $e^{i(\mathbf{k}-\mathbf{Q})\cdot\mathbf{r}}$, $H_{\mathbf{Q},\mathbf{Q}'}(\mathbf{k}) = \int d^2\mathbf{r} e^{-i(\mathbf{k}-\mathbf{Q})\cdot\mathbf{r}} H_0(\mathbf{r}) e^{i(\mathbf{k}-\mathbf{Q}')\cdot\mathbf{r}} / A$, to find:

$$H_{\mathbf{Q},\mathbf{Q}'}(\mathbf{k}) = \delta_{\mathbf{Q},\mathbf{Q}'} v_F \mathbf{z} \cdot [(\mathbf{k} - \mathbf{Q}) \times \boldsymbol{\sigma}] + w \sum_{j=1}^3 (\delta_{\mathbf{Q}'-\mathbf{Q},\mathbf{q}_j} + \delta_{\mathbf{Q}-\mathbf{Q}',\mathbf{q}_j}), \quad (3)$$

where $\mathbf{Q} = n_1\mathbf{g}_1 + n_2\mathbf{g}_2$ is a reciprocal lattice vector and $\mathbf{g}_1 = \mathbf{q}_2$ and $\mathbf{g}_2 = \mathbf{q}_3$ form a basis for the reciprocal lattice. We denote by $|u_{n\mathbf{k}}\rangle$ and $\epsilon_{n\mathbf{k}}$ the eigenstates and eigenvalues of $H_0(\mathbf{r})$, which in practice are obtained by diagonalizing Eq. (3).

Symmetries.— Here we briefly discuss the symmetries of $H_0(\mathbf{r})$ which incorporates the spin-momentum locked Dirac cone and the moiré potential. The model is invariant under time-reversal symmetry, $T H_0(\mathbf{r}) T^{-1} = H_0(\mathbf{r})$, with $T = \sigma_y K$, where K is the complex conjugation operator. The model is also invariant under the mirror symmetries $m_x : (x, y, z) \rightarrow (-x, y, z)$,

$$m_x H_0(\mathbf{r}) m_x^{-1} = H_0(-x, y),$$

and $m_y : (x, y, z) \rightarrow (x, -y, z)$,

$$m_y H_0(\mathbf{r}) m_y^{-1} = H_0(x, -y),$$

that are given by $m_x = \sigma_x$ and $m_y = \sigma_y$. Note that the product of m_x and m_y implies invariance under $C_{2z} : (x, y, z) \rightarrow (-x, -y, z)$, which is implemented by the σ_z matrix. In addition $H_0(\mathbf{r})$ commutes with C_{3z}

$$C_{3z} H_0(\mathbf{r}) C_{3z}^{-1} = H_0(C_{3z}\mathbf{r}),$$

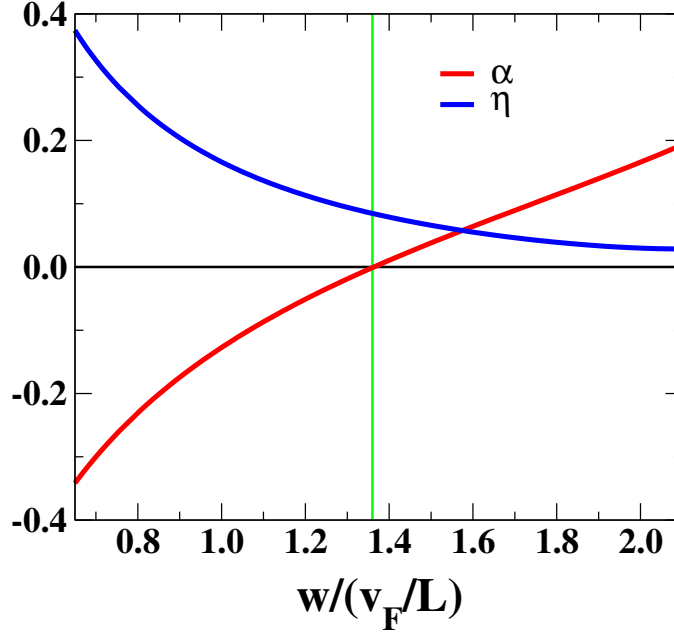


Figure 1. Parameters α and η of the $\mathbf{k} \cdot \mathbf{p}$ expansion of the dispersion relation around \mathbf{K} . The vanishing of α at $w/(v_F/L) = 1.36$ highlighted by the green line implies a HOVHS.

where $C_{3z} = \exp(2\pi i \sigma_z/3)$ is the three-fold spin rotation about the \mathbf{z} -axis. Notice that C_{2z} and m_y are symmetries of the low-energy model but not symmetries of the surface of materials in the Bi_2Se_3 family; including higher-order corrections to the linear Dirac cone reduces the symmetries of the model to those of surface states in Bi_2Se_3 [3].

Higher-order van Hove singularity.— The origin of the high order van Hove singularities (HOVHS) [4–7] can be derived from the lattice symmetries of the Hamiltonian $H_0(\mathbf{r})$. We define the small deviation from the \mathbf{K} point, $\mathbf{q} = \mathbf{k} - \mathbf{K}$, and the linear combinations $q_{\pm} = q_x \pm iq_y$, which transforms under C_{3z} as $q_{\pm} \rightarrow e^{\pm i2\pi/3} q_{\pm}$. At second order in \mathbf{q} the only allowed term in the energy dispersion is $q_+ q_- = q^2$. The next contributions invariant under C_{3z} are q_+^3 and q_-^3 . As a consequence of the mirror m_y symmetry the cubic term is $(q_+^3 + q_-^3)/2 = q_x^3 - 3q_x q_y^2$. Thus, to cubic order in \mathbf{q} the dispersion around \mathbf{K} reads [8] $\epsilon_{\mathbf{K}}(\mathbf{q}) = \epsilon_0 + \alpha q^2 + \eta(q_x^3 - 3q_x q_y^2) + \dots$. Applying time-reversal symmetry we find that the expansion at \mathbf{K}' reads $\epsilon_{\mathbf{K}'}(\mathbf{q}) \simeq \epsilon_0 + \alpha q^2 - \eta(q_x^3 - 3q_x q_y^2)$. The values of the coefficients α and η are obtained from the $\mathbf{k} \cdot \mathbf{p}$ perturbation theory at \mathbf{K} . Given $H_0(\mathbf{K} + \mathbf{q}) - H_0(\mathbf{K})$ expanding to the third order in the small deviation $\mathbf{q} = \mathbf{k} - \mathbf{K}$ yields:

$$\alpha = 2 \sum_{m \neq n} \frac{\text{Re}[\langle u_{n\mathbf{K}} | \sigma_+ | u_{m\mathbf{K}} \rangle \langle u_{m\mathbf{K}} | \sigma_- | u_{n\mathbf{K}} \rangle]}{\epsilon_{n\mathbf{K}} - \epsilon_{m\mathbf{K}}}, \quad (4)$$

and

$$\eta = \sum_{m, j \neq n} 2 \text{Im} \left[\frac{\langle u_{n\mathbf{K}} | \sigma_- | u_{m\mathbf{K}} \rangle \langle u_{m\mathbf{K}} | \sigma_- | u_{j\mathbf{K}} \rangle \langle u_{j\mathbf{K}} | \sigma_- | u_{n\mathbf{K}} \rangle}{(\epsilon_{n\mathbf{K}} - \epsilon_{m\mathbf{K}})(\epsilon_{n\mathbf{K}} - \epsilon_{j\mathbf{K}})} \right], \quad (5)$$

where $|u_{n\mathbf{K}}\rangle$ and $\epsilon_{n\mathbf{K}}$ are the Bloch state and the eigenvalue, respectively, of $H_0(\mathbf{r})$ at \mathbf{K} , n is the first positive energy band and $\sigma_{\pm} = \sigma_x \pm i\sigma_y$. The evolution of the couplings α and η is shown in Fig. 1. The higher-order van Hove singularity occurs when the quadratic term α in Eq. (4) vanishes at $w/(v_F/L) \simeq 1.36$, highlighted by the vertical green line in Fig. 1. The result is a power-law divergence in the density of states $\rho(\epsilon) \sim |\epsilon|^{-1/3}$. Moreover, by employing the $\mathbf{k} \cdot \mathbf{p}$ theory we can determine the position of the saddle points (i.e. VHSs) around \mathbf{K} and \mathbf{K}' . By looking at the solutions of $\nabla_{\mathbf{q}} \epsilon_{\pm}(\mathbf{q}) = 0$ (\pm for \mathbf{K} and \mathbf{K}' respectively), we find that $\mathbf{q} = 0$ is a maximum for $\alpha < 0$, a minimum for $\alpha > 0$ and, finally, a higher-order critical point for $\alpha = 0$. Away from the origin there are three further solutions at $\kappa_{\pm, j} = \mp 2\alpha C_{3z}^{j-1}(1, 0)/3\eta$, which are saddle points. Approaching the higher-order VHS at $\alpha \rightarrow 0$, these three saddle points merge at $\mathbf{q} = 0$, i.e., at \mathbf{K} or \mathbf{K}' . (Since the solutions for the saddle points are obtained for small \mathbf{q} , the values obtained for κ_j will break down when α/η is large, indicating that corrections higher than the cubic order in the dispersion are non negligible.)

Hexagonal Fermi surface warping.— Constrained by the crystal symmetries and time-reversal, the $\mathbf{k} \cdot \mathbf{p}$ theory

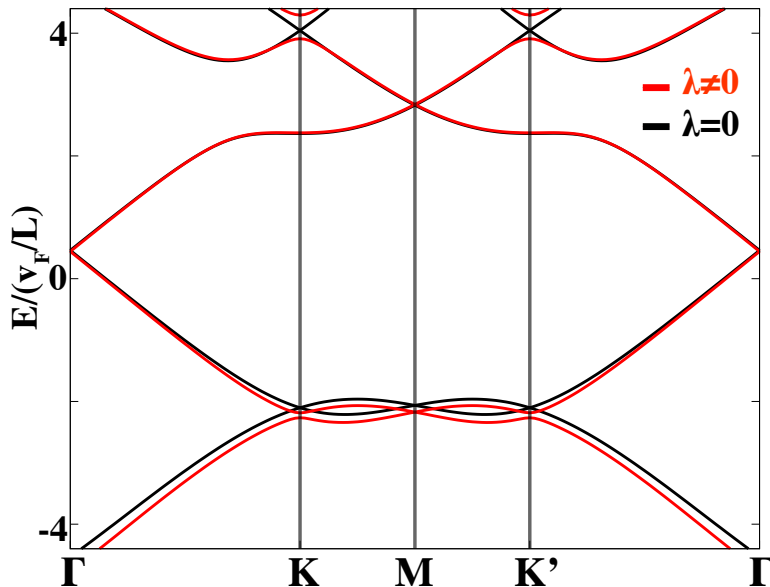


Figure 2. Red and black lines show the spectrum for $\lambda \neq 0$ and $\lambda = 0$ respectively. The calculation has been performed by setting $w/(v_F/L) \simeq 1.54$, $v_F = 2.55\text{eV}\text{\AA}$ and $\lambda = 250\text{eV}\text{\AA}^3$.

around the Dirac cone can be expanded beyond the linear term of $H_0(\mathbf{r})$ in Eq. (1). The next leading terms are [3]:

$$\delta H(\mathbf{k}) = \frac{k_+ k_-}{2m^*} \sigma_0 + \frac{\lambda}{2} (k_+^3 + k_-^3) \sigma_z, \quad (6)$$

with $k_{\pm} = k_x \pm ik_y$. The quadratic term gives rise to a particle-hole asymmetry without breaking any crystal-symmetry. The cubic term, $H_w(\mathbf{k}) = \lambda(k_+^3 + k_-^3)\sigma_z/2$, breaks C_{2z} but preserves the time-reversal symmetry T . In addition, we observe that higher order corrections (6) are small in $1/L$. In particular, we have that quadratic term is small in $4\pi/(\sqrt{3}m^*v_FL)$ while the hexagonal warping term goes like $(4\pi)^2\lambda/(3v_FL^2)$. We show the effect of the hexagonal warping on the band structure of the normal state in Fig. 2. The first band above charge neutrality is almost unchanged. Higher bands are more affected by the cubic correction. In particular, H_w has nodal lines along directions $\phi = \pi/6 + n\pi/3$ which preserves Dirac cones at Γ and \mathbf{M} , while is finite along $\phi = n\pi/3$, explaining the gap at \mathbf{K} and \mathbf{K}' in Fig. 2.

The screening of the Coulomb interaction in moiré surface states. — In this paragraph we discuss the screening of the Coulomb interaction by the surface electrons. In 2D the Fourier transform of the Coulomb potential $U(\mathbf{r}) = e^2/4\pi\epsilon_0\epsilon r$ is given by:

$$U(\mathbf{q}) = \int d^2\mathbf{r} e^{-i\mathbf{q}\cdot\mathbf{r}} U(\mathbf{r}) = \frac{e^2}{4\pi\epsilon_0\epsilon q}. \quad (7)$$

Within the Random phase approximation (RPA) the dressed Coulomb interaction reads:

$$U_*(\mathbf{q}, i\omega) = [1 - U(\mathbf{q})\Pi_0(\mathbf{q}, i\omega)]^{-1} U(\mathbf{q}). \quad (8)$$

Here Π_0 is the bare density-density response:

$$\Pi_0(\mathbf{q}, i\omega) = \frac{T}{V} \sum_{\mathbf{k}} \sum_{i\epsilon} \text{Tr} [G_0(\mathbf{k} + \mathbf{q}, i\omega + i\epsilon) G_0(\mathbf{k}, i\epsilon)], \quad (9)$$

where the bare Green's function G_0 of the surface electrons is simply:

$$G_0(\mathbf{k}, i\epsilon) = \sum_n \frac{|u_{n\mathbf{k}}\rangle \langle u_{n\mathbf{k}}|}{i\omega - \epsilon_{n\mathbf{k}}}. \quad (10)$$

In the static limit $\omega \rightarrow 0$ the density-density response function reads:

$$\Pi_0(\mathbf{q}, 0) = \frac{1}{A} \sum_{\mathbf{k}} \sum_{m, m'} \frac{f(\xi_{m\mathbf{k}}) - f(\xi_{m'\mathbf{k}+\mathbf{q}})}{\xi_{m\mathbf{k}} - \xi_{m'\mathbf{k}+\mathbf{q}}} |\langle u_{m\mathbf{k}} | u_{m'\mathbf{k}+\mathbf{q}} \rangle|^2, \quad (11)$$

where as usual we take the principal value of the integral. Before going on we notice that we can introduce the momentum-dependent Thomas-Fermi screening length:

$$\lambda_{\mathbf{q}}^{-1} = -e^2 \Pi_0(\mathbf{q}, 0) / (4\pi\epsilon_0\epsilon), \quad (12)$$

so that Eq. (8) in the static limit becomes:

$$U_*(\mathbf{q}, 0) = U(\mathbf{q}) \frac{1}{1 + 1/(q\lambda_{\mathbf{q}})}. \quad (13)$$

If we now take the quasi-homogeneous limit $\mathbf{q} \ll 1/L$ Eq. (11) simplifies considerably. First of all, we have that $\langle u_{m\mathbf{k}} | u_{m'\mathbf{k}} \rangle = \delta_{m, m'}$ and only states close to the Fermi level contribute. By taking the zero temperature limit ($T \rightarrow 0$) we obtain $\Pi_0(\mathbf{q} \ll 1/L, 0) = -\rho_F/\Omega$ where ρ_F is the density of states at the Fermi level and Ω is the area of the Moiré' unit cell. In this limit we find that the screening length is given by the standard expression $\lambda_{\mathbf{q} \ll 1/L}^{-1} = e^2 \rho_F / (4\pi\epsilon_0\epsilon\Omega)$ that gives the screened interaction:

$$U_*(\mathbf{q} \ll 1/L, 0) = \Omega/\rho_F. \quad (14)$$

A critical Fermi surface with a VHS is characterized by $\rho_F \rightarrow \infty$ that implies the suppression of the interaction $U_*(\mathbf{q} \ll 1/L, 0) \rightarrow 0$. The result changes considerably if we consider the wave vectors modulation $\mathbf{q} = \boldsymbol{\delta}_j = C_{3z}^{j-1}(\mathbf{K}' - \mathbf{K})$. In this case the screening length in Eq. (12) becomes:

$$\lambda_*^{-1} = -\frac{e^2}{4\pi\epsilon_0\epsilon\Omega} \frac{1}{N} \sum_{\mathbf{k}} \sum_{m, m'} \frac{f(\xi_{m\mathbf{k}}) - f(\xi_{m'\mathbf{k}+\boldsymbol{\delta}_j})}{\xi_{m\mathbf{k}} - \xi_{m'\mathbf{k}+\boldsymbol{\delta}_j}} |\langle u_{m\mathbf{k}} | u_{m'\mathbf{k}+\boldsymbol{\delta}_j} \rangle|^2, \quad (15)$$

where $\boldsymbol{\delta}_j$ is the modulation of the magnetic instability and λ_* does not depend on j as a result of the C_{3z} symmetry. The Coulomb interaction for $\mathbf{q} = \boldsymbol{\delta}_j$ is rescaled as:

$$U \rightarrow U_*/U = K(n), \quad K(n) = \left[1 + \frac{3L}{4\pi\lambda_*} \right]^{-1}, \quad (16)$$

where L is the superlattice length scale and n is the filling per moiré unit cell. We compute numerically the screening effect of the intraband contribution ($m' = m$ in Eq. (15)). The latter one is the dominant contribution close to the VHS filling. Indeed, interband transitions ($m' \neq m$) are going only to give small correction, which depends weakly on the temperature and on the value of the chemical potential. As a result we do not expect that the latter contribution changes the qualitative properties of our phase diagrams. Fig. 3 shows the renormalization of the interaction $K(n)$ in Eq. (16) as a function of the number of electrons. The screening of the interaction does not change the value of U drastically, we always find that $U_*/U \geq 0.93$. Finally, Fig. 4 shows the critical value of the interaction U_c (red line) for $T = 1.5\text{K}$, the bare (black) and the screened (blue) Coulomb interactions. The screening reduces the interval of instability from $n_c = [0.67, 0.76]$ to $n_{c,*} = [0.68, 0.75]$. Thus, despite the critical Fermi surface we find a regular density-density response function at $\boldsymbol{\delta}_j = C_{3z}^{j-1}(\mathbf{K}' - \mathbf{K})$ that slightly renormalizes the bare U . The result can be explained observing that the singularity coming from the large density of states at \mathbf{K} and \mathbf{K}' is removed by the vanishing overlap $|\langle u_{\mathbf{K}} | u_{\mathbf{K}'} \rangle| = 0$ in Eq. (15). This result applied to the attractive case ($U < 0$) implies the absence of the charge density wave instability as already pointed out in Ref. [8].

Mean field Hamiltonian. — We study the mean-field Hamiltonian:

$$H_{\text{MF}}(\mathbf{r}) = H_0(\mathbf{r}) - U \mathbf{m}(\mathbf{r}) \cdot \boldsymbol{\sigma} / 2, \quad (17)$$

where the order parameter $\mathbf{m}(\mathbf{r})$ is given by:

$$\mathbf{m}(\mathbf{r}) = \sum_{j, \mu=1}^3 (e^{i\boldsymbol{\delta}_j \mathbf{r}} s_{\mu j} \mathbf{v}_{\mu j} + e^{-i\boldsymbol{\delta}_j \mathbf{r}} s_{\mu j}^* \mathbf{v}_{\mu j}^*), \quad (18)$$

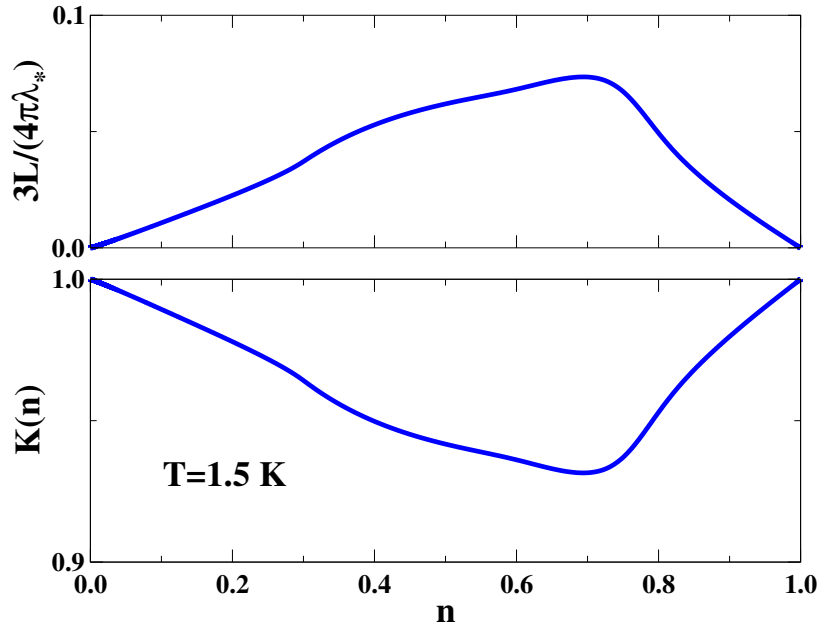


Figure 3. Top panel: Thomas-Fermi screening length. Bottom panel: screening of the Coulomb interaction $K(n)$ as a function of the number of electron per moiré unit cell n . The calculation has been performed by setting $w/(v_F/L) \simeq 1.54$, $v_F = 2.55\text{eV}\text{\AA}$, and $T = 1.5\text{K}$.

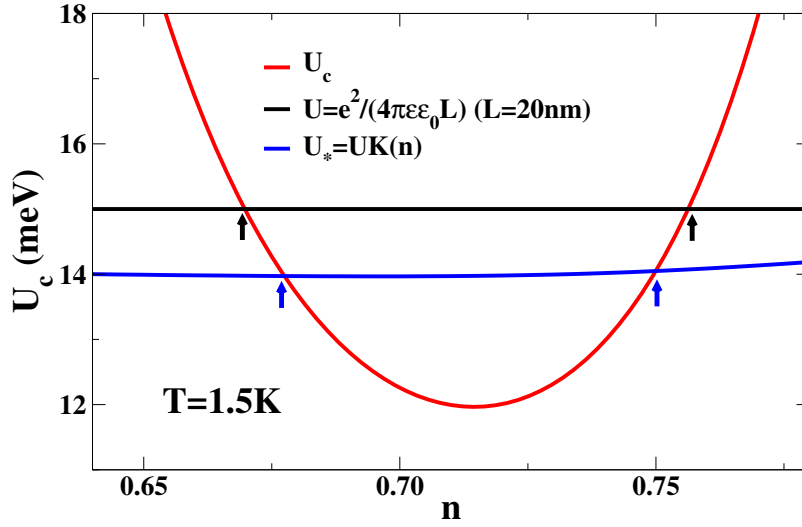


Figure 4. The red solid line shows the critical value of the interaction above which the instability takes place. Black and blue lines denote the bare and the screened Coulomb interaction, respectively. The calculation has been performed by setting $w/(v_F/L) \simeq 1.54$, $v_F = 2.55\text{eV}\text{\AA}$, and $T = 1.5\text{K}$.

with δ_j given by

$$\delta_j = \frac{4\pi}{3L} \left(\cos \frac{2\pi j}{3}, \sin \frac{2\pi j}{3} \right), \quad (19)$$

and $\mathbf{v}_{\mu j}$ defined as

$$\mathbf{v}_{\parallel j} = \mathbf{e}_j \equiv \delta_j / |\delta_j|, \quad \mathbf{v}_{\perp j} = -i(\mathbf{z} \times \mathbf{e}_j), \quad \mathbf{v}_{zj} = -i\mathbf{z}. \quad (20)$$

In the plane wave basis, defined above Eq. (3):

$$H_{\text{HF},\mathbf{Q}\mathbf{Q}'}(\mathbf{k}) = \delta_{\mathbf{Q},\mathbf{Q}'} v_F \mathbf{z} \cdot [(\mathbf{k} - \mathbf{Q}) \times \boldsymbol{\sigma}] + w\sigma_0 \sum_{j=1}^3 (\delta_{\mathbf{Q}'-\mathbf{Q},\mathbf{q}_j} + \delta_{\mathbf{Q}-\mathbf{Q}',\mathbf{q}_j}) - \frac{U}{2} \sum_{j=1,\mu}^3 \left(s_{\mu j} O_{\mu j} \delta_{\mathbf{Q}'-\mathbf{Q},\boldsymbol{\delta}_j} + s_{\mu j}^* O_{\mu j}^\dagger \delta_{\mathbf{Q}-\mathbf{Q}',\boldsymbol{\delta}_j} \right), \quad (21)$$

where $O_{\nu j} = \mathbf{v}_{\nu j} \cdot \boldsymbol{\sigma}$.

II. SYMMETRY TRANSFORMATIONS OF THE SDW OPERATOR

Transformations of the order parameter— Here we examine the effect of the symmetries of the Hamiltonian on the spin density wave operators $\hat{S}_{\mu j}$ that, we remind, are given by:

$$\hat{S}_{\mu j} = \sum_{\mathbf{k}} \sum_{\mathbf{G}} \hat{c}_{\mathbf{k}+\boldsymbol{\delta}_j,\mathbf{G},\sigma}^\dagger \mathbf{v}_{\mu j} \cdot \boldsymbol{\sigma}_{\sigma\sigma'} \hat{c}_{\mathbf{k},\mathbf{G},\sigma'}. \quad (22)$$

We start by recalling the transformation rules of a fermionic operator under the element g of the symmetry group composed by C_{3z} , $m_{x/y}$ and T , $g c_{\mathbf{k},\mathbf{Q},\sigma}^\dagger g^{-1} = c_{g\mathbf{k},g\mathbf{Q},\sigma'}^\dagger D(g)_{\sigma'\sigma}$, where $D(g)$ is the representation of the symmetry in the two-fold degenerate manifold at $\mathbf{\Gamma}$:

$$D(C_{3z}) = e^{\frac{2\pi i \sigma_z}{3}}, \quad D(m_{x/y}) = \sigma_{x/y}, \quad D(T) = \sigma_y K. \quad (23)$$

We start by examining C_{3z} :

$$C_{3z} \hat{S}_{\mu j} C_{3z}^{-1} = \sum_{\mathbf{k}} \sum_{\mathbf{Q}} \hat{c}_{\mathbf{k}+\boldsymbol{\delta}_{j+1},\mathbf{Q},\sigma}^\dagger \left[e^{2\pi i \sigma_z/3} \mathbf{v}_{\mu j} \cdot \boldsymbol{\sigma} e^{-2\pi i \sigma_z/3} \right]_{\sigma\sigma'} \hat{c}_{\mathbf{k},\mathbf{G},\sigma'} \\ = \sum_{\mathbf{k}} \sum_{\mathbf{Q}} \hat{c}_{\mathbf{k}+\boldsymbol{\delta}_{j+1},\mathbf{Q},\sigma}^\dagger [R_{2\pi/3} \mathbf{v}_{\mu j} \cdot \boldsymbol{\sigma}]_{\sigma\sigma'} \hat{c}_{\mathbf{k},\mathbf{Q},\sigma'} = \hat{S}_{\mu j+1}, \quad (24)$$

where we have used the relation $R_{2\pi/3} \mathbf{v}_{\mu j} = \mathbf{v}_{\mu j+1}$. For m_x :

$$m_x \hat{S}_{\mu j} m_x^{-1} = \sum_{\mathbf{k}} \sum_{\mathbf{Q}} \hat{c}_{\mathbf{k}+m_x \boldsymbol{\delta}_j,\mathbf{Q},\sigma}^\dagger [\sigma_x \mathbf{v}_{\mu j} \cdot \boldsymbol{\sigma} \sigma_x]_{\sigma\sigma'} \hat{c}_{\mathbf{k},\mathbf{Q},\sigma'} \\ = \sum_{\mathbf{k}} \sum_{\mathbf{Q}} \hat{c}_{\mathbf{k}+m_x \boldsymbol{\delta}_j,\mathbf{Q},\sigma}^\dagger [M \mathbf{v}_{\mu j} \cdot \boldsymbol{\sigma}]_{\sigma\sigma'} \hat{c}_{\mathbf{q},\mathbf{Q},\sigma'}, \quad (25)$$

where M transforms $(a, b, c) \rightarrow (a, -b, -c)$. By using the properties of $\mathbf{v}_{\mu j}$ and knowing how $\boldsymbol{\delta}_j$ transforms under m_x we find:

$$m_x \hat{S}_{\mu 1} m_x^{-1} = \hat{S}_{\mu 1}^\dagger, \quad m_x \hat{S}_{\mu 2} m_x^{-1} = \hat{S}_{\mu 3}^\dagger. \quad (26)$$

In addition, we have the mirror m_y symmetry:

$$m_y \hat{S}_{\mu j} m_y^{-1} = \sum_{\mathbf{k}} \sum_{\mathbf{Q}} \hat{c}_{\mathbf{k}+m_y \boldsymbol{\delta}_j,\mathbf{Q},\sigma}^\dagger [\sigma_y \mathbf{v}_{\mu j} \cdot \boldsymbol{\sigma} \sigma_y]_{\sigma\sigma'} \hat{c}_{\mathbf{k},\mathbf{Q},\sigma'} \\ = \sum_{\mathbf{k}} \sum_{\mathbf{Q}} \hat{c}_{\mathbf{k}+m_y \boldsymbol{\delta}_j,\mathbf{Q},\sigma}^\dagger [\tilde{M} \mathbf{v}_{\mu j} \cdot \boldsymbol{\sigma}]_{\sigma\sigma'} \hat{c}_{\mathbf{k},\mathbf{Q},\sigma'}, \quad (27)$$

where the matrix \tilde{M} acts on the components of the vector $\mathbf{v}_{\mu j}$ as $\tilde{M} : (a, b, c) \rightarrow (-a, b, -c)$. Thus, we obtain for $\mu = \parallel, z$:

$$m_y \hat{S}_{\mu 1} m_y^{-1} = -\hat{S}_{\mu 1}, \quad m_y \hat{S}_{\mu 2} m_y^{-1} = -\hat{S}_{\mu 3}, \quad (28)$$

and for $\mu = \perp$

$$m_y \hat{S}_{\perp 1} m_y^{-1} = \hat{S}_{\perp 1}, \quad m_y \hat{S}_{\perp 2} m_y^{-1} = \hat{S}_{\perp 3}. \quad (29)$$

Finally, under time reversal symmetry:

$$T \hat{S}_{\mu j} T^{-1} = \sum_{\mathbf{k}, \mathbf{Q}} \hat{c}_{-\mathbf{k}-\delta_j, -\mathbf{Q}, \sigma}^\dagger [\mathbf{v}_{\mu j}^* \cdot \sigma^y \boldsymbol{\sigma}^* \sigma^y]_{\sigma \sigma'} \hat{c}_{-\mathbf{k}, -\mathbf{Q}, \sigma'} = - \sum_{\mathbf{k}, \mathbf{Q}} \hat{c}_{\mathbf{k}, \mathbf{Q}, \sigma}^\dagger [\mathbf{v}_{\mu j}^* \cdot \boldsymbol{\sigma}]_{\sigma \sigma'} \hat{c}_{\mathbf{k}+\delta_j, \mathbf{Q}, \sigma'} = -\hat{S}_{\mu j}^\dagger. \quad (30)$$

We are going to employ in Sec. IV the previous symmetries to constraint the form of the Ginzburg-Landau free energy.

III. HUBBARD-STRATONOVICH TRANSFORMATION AND SADDLE-POINT EQUATIONS

From H_0 (1) and the local Hubbard repulsion,

$$\hat{H}_{\text{int}} = U \int d^2 \mathbf{r} \hat{\Psi}_\uparrow^\dagger(\mathbf{r}) \hat{\Psi}_\downarrow^\dagger(\mathbf{r}) \hat{\Psi}_\downarrow(\mathbf{r}) \hat{\Psi}_\uparrow(\mathbf{r}); \quad U > 0, \quad (31)$$

follows the finite-temperature action:

$$S = \int_0^\beta d\tau \left[\sum_{n\mathbf{k}} \bar{\psi}_{n\mathbf{k}}(\tau) (\partial_\tau + E_{n\mathbf{k}} - \mu) \psi_{n\mathbf{k}}(\tau) + \frac{U}{4} \int d^2 \mathbf{r} \rho(\mathbf{r}) \rho(\mathbf{r}) - \frac{U}{4} \int d^2 \mathbf{r} \mathbf{S}(\tau, \mathbf{r}) \cdot \mathbf{S}(\tau, \mathbf{r}) \right], \quad (32)$$

where $\bar{\psi}_{n\mathbf{k}}(\tau)$ and $\psi_{n\mathbf{k}}(\tau)$ are now Grassmann variables in the basis of the eigenstates of $H_0(\mathbf{r})$, and β is the inverse temperature $\beta = 1/k_B T$. In Eq. (32) we express the local interaction in terms of the spin and charge density operators [9] that we define as $\hat{\rho}(\mathbf{r}) = \sum_\sigma \hat{\Psi}_\sigma^\dagger(\mathbf{r}) \hat{\Psi}_\sigma(\mathbf{r})$ and $\hat{S}_a(\mathbf{r}) = \hat{\Psi}^\dagger(\mathbf{r}) \sigma_a \hat{\Psi}(\mathbf{r})$ with $\hat{\Psi}_\sigma(\mathbf{r})$ the field operator annihilating an electron with spin $\sigma = (\uparrow, \downarrow)$ at \mathbf{r} . By performing the Hubbard-Stratonovich transformation [10–12] on the charge $\rho(\mathbf{r})$ and the spin $\mathbf{S}(\mathbf{r})$ we find:

$$S_{HS}[n, \mathbf{m}] = \int_0^\beta d\tau \left[\sum_{n\mathbf{k}} \bar{\psi}_{n\mathbf{k}}(\tau) (\partial_\tau + E_{n\mathbf{k}} - \mu) \psi_{n\mathbf{k}}(\tau) + \frac{U}{2} \int d^2 \mathbf{r} n(\tau, \mathbf{r}) \rho(\tau, \mathbf{r}) - \frac{U}{2} \int d^2 \mathbf{r} \mathbf{m}(\tau, \mathbf{r}) \cdot \mathbf{S}(\tau, \mathbf{r}) \right. \\ \left. + \frac{U}{4} \int d^2 \mathbf{r} \mathbf{m}^2(\tau, \mathbf{r}) - \frac{U}{4} \int d^2 \mathbf{r} n^2(\tau, \mathbf{r}) \right], \quad (33)$$

where we have introduced two bosonic fields $\mathbf{m}(\tau, \mathbf{r})$ and $n(\tau, \mathbf{r})$. Finally, by integrating out the electronic degrees of freedom we obtain the effective action for $n(\tau, \mathbf{r})$ and $\mathbf{m}(\tau, \mathbf{r})$:

$$S[n, \mathbf{m}] = \frac{U}{4} \int_0^\beta d\tau \int d^2 \mathbf{r} [\mathbf{m}^2(\tau, \mathbf{r}) - n^2(\tau, \mathbf{r})] + \text{Tr} \left[\sum_{n=1}^\infty \frac{(-G_0 X)^n}{n} \right], \quad (34)$$

where $G_0^{-1} = -\partial_\tau - H_0 + \mu$ is the non-interacting Green's function and $X = U \mathbf{m}(\tau, \mathbf{r}) \boldsymbol{\sigma} / 2 - U n(\tau, \mathbf{r}) / 2$. As a consequence of the sign difference a local repulsive interaction gives rise to magnetic instabilities and favours a homogeneous charge distribution. Moreover, a charge-density-wave (CDW), characterized by a finite expectation value of

$$\langle \rho_{\mathbf{q}} \rangle = \frac{1}{A} \sum_{\mathbf{k}} \sum_{\mathbf{Q}} \sum_{\sigma} \langle c_{\mathbf{k}+\mathbf{q}, \mathbf{Q}, \sigma}^\dagger c_{\mathbf{k}, \mathbf{Q}, \sigma} \rangle \neq 0, \quad (35)$$

forces the electrons to have the same spin orientation. However, due to the spin-momentum locking it is unfavorable to have a large expectation value of $c_{\mathbf{k}+\mathbf{q}, \mathbf{Q}, \sigma}^\dagger c_{\mathbf{k}, \mathbf{Q}, \sigma}$ on the Bloch states $|u_{n\mathbf{k}}\rangle$ of $H_0(\mathbf{r})$ (1). Thus, a CDW order is unlikely in superlattice tuned TI surface states.

By taking the semi-classical limit of a static order parameter we obtain the free energy:

$$F = \frac{A}{2} \left(\sum_{\mu j} |s_{\mu j}|^2 - \frac{n^2}{2} \right) + \sum_{m=1}^\infty \text{Tr} \left[\frac{(-G_0 X)^m}{m U} \right]. \quad (36)$$

Minimizing F (36) with respect to the filling n and the magnetic configurations $\mathbf{m}(\mathbf{r})$ we find the saddle-point equations:

$$\frac{\delta F}{\delta n} = 0 \Rightarrow n = \frac{1}{A} \text{Tr} \left[(G_0^{-1} + X)^{-1} \right], \quad (37)$$

and

$$\frac{\delta F}{\delta s_{\mu j}^*} = 0 \Rightarrow s_{\mu j} = \frac{2}{UA} \text{Tr} \left[\frac{\delta X}{\delta s_{\mu j}^*} (G_0^{-1} + X)^{-1} \right]. \quad (38)$$

In the main text we show the result of the numerical solution of Eqs. (37) and (38), which was obtained as follows. Eqs. (37) and (38) take a simple form in the basis of the eigenstates $|\phi_{n\mathbf{k}}\rangle$ of the Hartree-Fock Hamiltonian in Eq. (21) with eigenvalues $\bar{\epsilon}_{n\mathbf{k}}$:

$$n = \frac{1}{3N} \sum_{n\mathbf{k}} f(\bar{\xi}_{n\mathbf{k}}) - n_0, \quad (39)$$

where $\bar{\xi}_{n\mathbf{k}} = \bar{\epsilon}_{n\mathbf{k}} - \mu^*$ and $\mu^* = \mu - Un/2$; and

$$s_{\mu j} = \frac{1}{3N} \sum_{n\mathbf{k}} f(\bar{\xi}_{n\mathbf{k}}) \langle \phi_{n\mathbf{k}} | O_{\mu j}^\dagger V^{\delta_j} | \phi_{n\mathbf{k}} \rangle, \quad (40)$$

where the filling n is measured with respect to the charge neutrality point n_0 , N is the number of points sampling the Brillouin zone, the factor of three takes into account the size difference between the original and the magnetic Brillouin zone, $f(\epsilon) = (e^{\beta\epsilon} + 1)^{-1}$ is the Fermi-Dirac distribution function, and $V^{\mathbf{G}}$ is the sewing matrix satisfying $V_{\mathbf{Q},\mathbf{Q}'}^{\mathbf{G}} = \delta_{\mathbf{Q},\mathbf{Q}'+\mathbf{G}}$, $V^{\mathbf{G}} |\phi_{n\mathbf{k}}\rangle = |\phi_{n\mathbf{k}+\mathbf{G}}\rangle$. The self-consistent solution of Eqs. (39) and (40) has been performed by restricting the sum over n in Eq. (40) to the first three ‘‘active’’ bands above charge neutrality. In a range of doping around $2/3$ filling and for reasonable values of the interaction the saddle-point solution of the free energy F given by Eqs. (37) and (38) gives a unique ground state that describes a skyrmion lattice where $s_{\mu j} = \xi_j U_\mu / \sqrt{3}$ with $\xi_j = \xi_{j+1}$ and $(U_\parallel, 0, U_z)$.

Evaluating the spin-susceptibility.— To find the instability condition, we linearise Eq. (38) in $s_{\mu j}$:

$$s_{\mu j} = -\frac{2}{UA} \text{Tr} \left[G_0 \frac{\delta X}{\delta s_{\mu j}^*} G_0 X \right] = \frac{U}{2} \sum_{\nu l} \chi_{jl}^{\mu\nu} s_{\nu l}, \quad (41)$$

which is the saddle-point equation of the quadratic free energy:

$$F_{(2)} = \sum_{\mu\nu} \sum_{jl} s_{\mu j}^* \left[\delta_{\mu\nu} - \frac{U}{2} \chi_{jl}^{\mu\nu} \right] s_{\nu l}, \quad (42)$$

with $\chi_{jl}^{\mu\nu}$ electronic susceptibility. As expected the magnetic instability takes place when the matrix in Eq. (42) $\mathcal{M} = \mathbf{1} - U\chi/2$ is not invertible, *i.e.*, $\det \mathcal{M} = 0$. Moreover, a negative eigenvalue of \mathcal{M} signals the formation of a SDW on the surface of the TI. We conclude the section by giving the expression of the susceptibility $\chi_{jl}^{\mu\nu}$:

$$\chi_{jl}^{\mu\nu} = -\frac{T}{A} \sum_{\mathbf{k}, \epsilon_n} \text{Tr} \left[G_0(\mathbf{k}, i\epsilon_n) O_{\mu j}^\dagger V^{\delta_j - \delta_l} G_0(\mathbf{k} + \delta_l, i\epsilon_n) O_{\nu l} \right], \quad (43)$$

where for simplicity we have introduced the operator $O_{\mu j} = \mathbf{v}_{\mu j} \cdot \boldsymbol{\sigma}$ and $V^{\mathbf{G}}$ is the sewing matrix $V_{\mathbf{Q},\mathbf{Q}'}^{\mathbf{G}} = \delta_{\mathbf{Q},\mathbf{Q}'+\mathbf{G}}$. For $j \neq l$ Eq. (43) describes Umklapp processes where the particle-hole excitation is scattered outside the Brillouin zone. We notice that Moreover, the non-interacting single particle Green’s function is given by:

$$G_0(\mathbf{k}, i\epsilon) = \sum_n \frac{|u_{n\mathbf{k}}\rangle \langle u_{n\mathbf{k}}|}{i\epsilon - \xi_{n\mathbf{k}}}, \quad (44)$$

where $|u_{n\mathbf{k}}\rangle$ are the Bloch eigenstates of H_0 and $\xi_{n\mathbf{k}}$ is the dispersion relation of H_0 measured with respect to the chemical potential $\xi_{n\mathbf{k}} = \epsilon_{n\mathbf{k}} - \mu$. By using (44) in (43) we readily find:

$$\chi_{jl}^{\mu\nu} = \frac{1}{2A} \sum_{\mathbf{k}} \sum_{n, n'} \frac{\tanh \frac{\beta \xi_{n'\mathbf{k}+\delta_l}}{2} - \tanh \frac{\beta \xi_{n\mathbf{k}}}{2}}{\xi_{n'\mathbf{k}+\delta_l} - \xi_{n\mathbf{k}}} \langle u_{n\mathbf{k}} | O_{\mu j}^\dagger V^{\delta_j - \delta_l} | u_{n'\mathbf{k}+\delta_l} \rangle \langle u_{n'\mathbf{k}+\delta_l} | O_{\nu l} | u_{n\mathbf{k}} \rangle. \quad (45)$$

Since the sums n and n' run over the whole spectrum of H_0 the evaluation of the interband contribution of Eq. (45) requires an ultraviolet regularization which has been implemented as explained in Refs. [13, 14]. Moreover, the

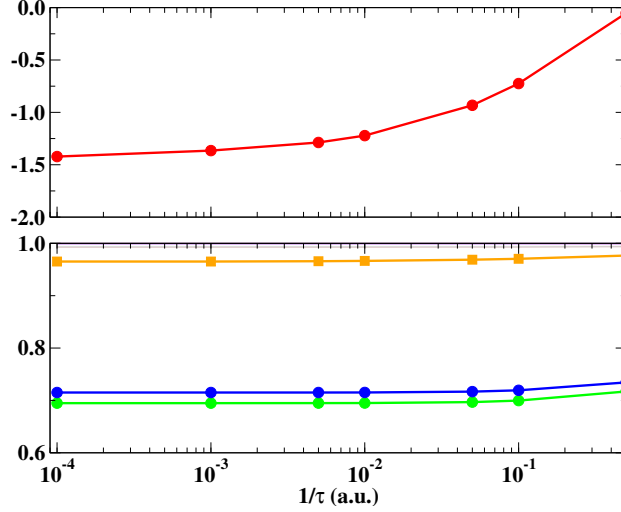


Figure 5. Convergence of the spectrum of $\delta_{\mu\nu} - U\chi_{jl}^{\mu\nu}/2$ as a function of \hbar/τ . In the top panel we show lowest eigenvalue of $\delta_{\mu\nu} - U\chi_{jl}^{\mu\nu}/2$ while in the bottom one the remaining eigenvalues. Calculations are performed with $L = 20\text{nm}$, $U = 30\text{meV}$, $w/(v_F/L) = 1.54$, $T = 1.5\text{K}$ and $\lambda = 250\text{eV}\text{\AA}^3$.

integrand of the intraband contribution $n = n'$ in Eq. (45) becomes ill-defined ($0/0$ indeterminate form) when $\epsilon_{n\mathbf{k}+\delta_l} = \epsilon_{n\mathbf{k}}$. The integrand has been regularized by taking the principal value:

$$\frac{1}{\epsilon_{n\mathbf{k}+\delta_l} - \epsilon_{n\mathbf{k}}} \rightarrow \frac{\xi_{n\mathbf{k}+\delta_l} - \xi_{n\mathbf{k}}}{(\xi_{n\mathbf{k}+\delta_l} - \xi_{n\mathbf{k}})^2 + (\hbar/\tau)^2}, \quad (46)$$

which corresponds to introduce an infrared cutoff \hbar/τ . Fig. 5 shows the evolution of the spectrum of the second order matrix $\delta_{\mu\nu} - U\chi_{jl}^{\mu\nu}/2$ as a function of \hbar/τ . The numerical result for $\chi_{jl}^{\mu\nu}$ is obtained for values of \hbar/τ where we reach a plateau.

IV. GINZBURG LANDAU THEORY

Symmetries of the second order matrix.—To determine the properties of $\mathcal{M}_{jl}^{\mu\nu}$ we employ the following symmetries: $C_{3z} : s_{\mu j} \rightarrow s_{\mu j+1}$, $m_x : s_{\mu 1} \rightarrow s_{\mu 1}^*$ and $m_x : s_{\mu 2} \rightarrow s_{\mu 3}^*$, $m_y : s_{\mu 1} \rightarrow -s_{\mu 1}$ and $m_y : s_{\mu 2} \rightarrow -s_{\mu 3}$ for $\mu = \parallel, z$ while for $\mu = \perp$ we have $m_y : s_{\perp 1} \rightarrow s_{\perp 1}$ and $m_y : s_{\perp 2} \rightarrow s_{\perp 3}$. The matrix is also invariant under time-reversal $T : s_{\mu j} \rightarrow s_{\mu j}^*$ and translation by moiré lattice vectors $T_{\mathbf{R}} : s_{\mu j} \rightarrow e^{i\delta_j \cdot \mathbf{R}} s_{\mu j}$, but these symmetries do not impose any additional constraints. The three-fold rotation $C_{3z} : s_{\mu j} \rightarrow s_{\mu j+1}$ (24) gives $\mathcal{M}_{jl}^{\mu\nu} = \mathcal{M}_{j+1l+1}^{\mu\nu}$. As a result $\mathcal{M}_{jl}^{\mu\nu}$ is expressed in terms of two three-dimensional matrices: $\Lambda_{\mu\nu} = \mathcal{M}_{j,j}^{\mu\nu}$, $\Omega_{\mu\nu} = \mathcal{M}_{j,j+1}^{\mu\nu}$ while $\mathcal{M}_{j+1,j}^{\mu\nu} = \Omega_{\nu\mu}^*$ since the free energy $F_{(2)}$ is real. In addition, the mirror symmetry m_x (26) implies that $\Lambda_{\mu\nu}$ is real and symmetric while $\Omega_{\mu\nu}$ symmetric $\Omega_{\mu\nu} = \Omega_{\nu\mu}$ but with complex elements $\Omega_{\mu\nu}^* \neq \Omega_{\nu\mu}$. Finally, the remaining m_y symmetry imposes that the matrix elements $\Lambda_{\parallel\perp} = 0$ and $\Lambda_{\perp z} = 0$, $\Omega_{\parallel\perp}$ and $\Omega_{\perp z}$ are purely imaginary, while the other components of $\Omega_{\mu\nu}$ are reals. The latter constraint implies that the C_{3z} symmetric spiral-xy order decouples from the 120-xy and out-of-plane orderings. Indeed, by projecting the second order free energy (42) on the C_{3z} symmetric configuration $s_{\mu j} = \xi U_{\mu}/\sqrt{3}$ we find:

$$F_{(2)} = \frac{|M|^2}{2} \sum_{\mu\nu} U_{\mu}^* [\Lambda_{\mu\nu} + 2 \text{Re} \Omega_{\mu\nu}] U_{\nu} = \frac{|M|^2}{2} \begin{pmatrix} U_{\parallel} \\ U_{\perp} \\ U_z \end{pmatrix}^{\dagger} \begin{pmatrix} L_{\parallel\parallel} & 0 & L_{\parallel z} \\ 0 & L_{\perp\perp} & 0 \\ L_{\parallel z} & 0 & L_{zz} \end{pmatrix} \begin{pmatrix} U_{\parallel} \\ U_{\perp} \\ U_z \end{pmatrix}, \quad (47)$$

where $L_{\mu\nu} = \Lambda_{\mu\nu} + 2 \text{Re} \Omega_{\mu\nu}$ and matrix vector product is assumed.

Symmetry classification of magnetic orderings and absence of competing magnetic instabilities.— In this section we discuss the spectrum of $\mathcal{M}_{jl}^{\mu\nu}$ and we classify the magnetic states with respect to their symmetry behaviour under the point-group symmetries of the free energy. The magnetic ordering is described by the real order parameter $\mathbf{m}(\mathbf{r}) = \sum_j \mathbf{m}_j e^{i\delta_j \cdot \mathbf{r}} + c.c.$ which is completely determined by the Fourier amplitudes $\mathbf{m}_j = \sum_{\mu} s_{\mu j} \mathbf{v}_{\mu j}$. To start with we recall the action of the symmetries on $s_{\mu j} = \langle \hat{S}_{\mu j} \rangle / A$: $C_{3z} : s_{\mu j} \rightarrow s_{\mu j+1}$; $m_x : s_{\mu 1} \rightarrow s_{\mu 1}^*$, $s_{\mu 2} \rightarrow s_{\mu 3}^*$;

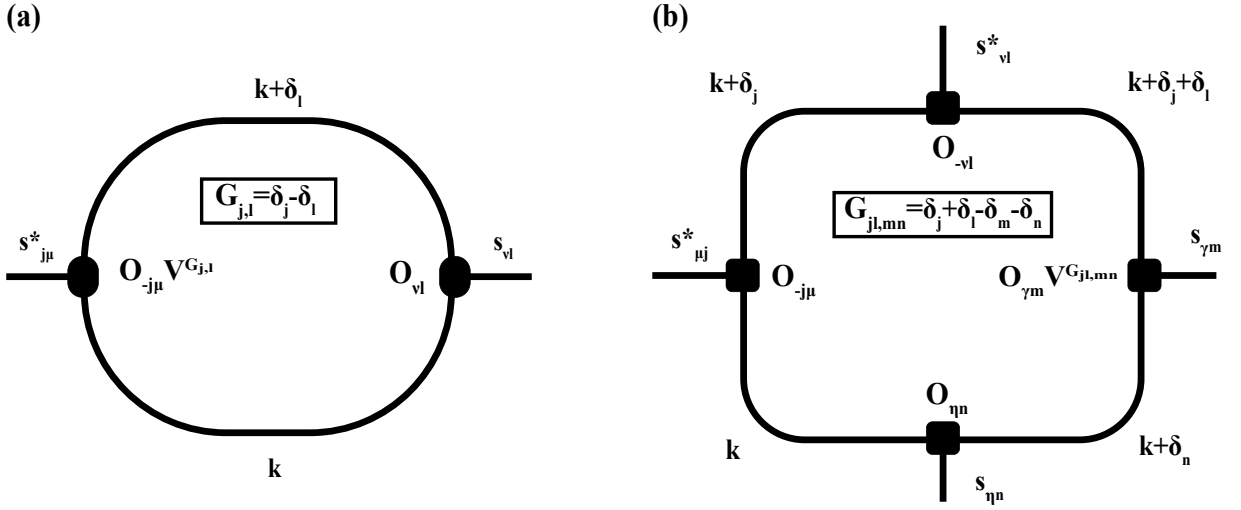


Figure 6. (a) Second order contribution to the magnetic free energy due to electron-hole spin excitations. (b) Fourth order contribution. The square box gives the moiré reciprocal lattice vector scattered by the fermionic loop.

	E	$2C_3$	$3m$
Γ_1	1	1	1
Γ_2	1	1	-1
Γ_3	2	-1	0

Table I. Character table of C_{3v} . E , C_3 and m represent the conjugation classes of the identity, C_{3z} and m_y , respectively.

$m_y : s_{\mu 1} \rightarrow -s_{\mu 1}, s_{\mu 2} \rightarrow -s_{\mu 3}$ for $\mu = \parallel, z$ and $m_y : s_{\perp 1} \rightarrow s_{\perp 1}, s_{\perp 2} \rightarrow s_{\perp 3}$. In addition, the free energy is also invariant under moiré lattice translations $T_{\mathbf{R}}$ with $\mathbf{R} = n_1 \mathbf{t}_1 + n_2 \mathbf{t}_2$, $n_{1,2} \in \mathbb{Z}$ and $\mathbf{t}_{1,2}$ primitive lattice vectors transforming the order parameter as $T_{\mathbf{R}} : s_{\mu j} \rightarrow e^{i\delta_j \cdot \mathbf{R}} s_{\mu j}$. The symmetries m_y and C_{3z} , that do not mix $s_{\mu j}$ and $s_{\mu j}^*$, generate the group C_{3v} whose characters are shown in Table I. The nine magnetic configurations originating from $s_{\mu j}$ are decomposed in one one-dimensional representation Γ_1 , two one-dimensional representations Γ_2 and three two-dimensional representations Γ_3 . The one-dimensional representations Γ_1 and Γ_2 are symmetric under C_{3z} and corresponds to equal superpositions of the modulations $\delta_{1,2,3}$. The parity of Γ_1 under m_y is even consistently with the spiral-xy order. On the other hand, Γ_2 is odd under m_y like the 120-xy and out-of-plane orderings. Due to the intrinsic spin-orbit coupling in-plane 120-xy and out-of-plane orderings mix to form the skyrmion lattice state. Finally, we have the two-dimensional representation Γ_3 . Here, we find two eigenstates of C_{3z} characterized by eigenvalues $\omega = e^{2\pi i/3}$ and ω^* and m_y is off-diagonal in this basis. Two dimensional degeneracy implies from this symmetry.

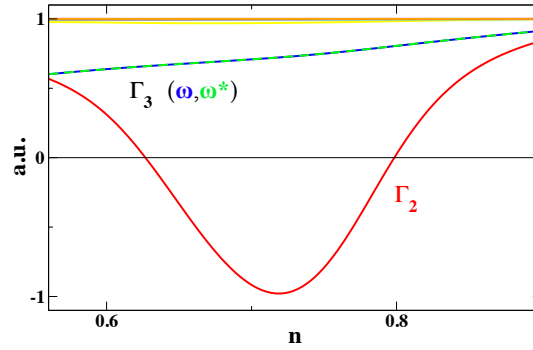


Figure 7. Spectrum of \mathcal{M} for $U = 30\text{meV}$, $2w = 40\text{meV}$, and $\beta v_F/L = .01$, which corresponds to $T \simeq 2\text{K}$ and $w/(v_F/L) \simeq 1.54$ for $L = 20\text{nm}$. The lowest eigenvalue, shown by the red line, is the only unstable magnetic ordering. The corresponding eigenstate transforms as the Γ_2 irrep and is a superposition of \parallel and z . The first excited state belongs to the Γ_3 and is composed of two degenerate states indicated by green and blue lines.

Data in Fig. 7 show the evolution of the spectrum of $\mathcal{M}_{jl}^{\mu\nu}$ as a function of the filling per moiré unit cell below the critical temperature. We find that the matrix has exactly one eigenvalue that becomes negative over a range of filling around the VHS red line in Fig. 7 giving rise to a magnetic instability. The corresponding eigenstate transforms as the irreducible representation Γ_2 : it is odd under m , is an equal superposition of the modulations δ_j , and has both \parallel and z components. Specifically, the order parameter $\mathbf{m}_j = \mathbf{m}_{j+1}$ takes the form $\mathbf{m}_j = |M|(U_{\parallel}\mathbf{v}_{\parallel j} + U_z\mathbf{v}_{zj})$. The first excited states transform as the two-dimensional irrep Γ_3 , taking the any linear combinations of the two degenerate states $\mathbf{m}_j = (\omega^*)^{j-1}|M|\sum_{\mu}U_{\mu}\mathbf{v}_{\mu j}$ and $\mathbf{m}_j = (\omega)^{j-1}|M|\sum_{\mu}U_{\mu}\mathbf{v}_{\mu j}$ with $\omega = e^{2i\pi/3}$. For completeness, we describe the remaining irrep in Table I, Γ_1 , which is an equal superposition of all δ_j but only has weight in the \perp component, $\mathbf{m}_j \propto \mathbf{v}_{\perp j}$.

The fourth order contribution.—We now consider the fourth order contribution from the expansion of the second term in Eq. (34). The corresponding vertex has four legs, labelled by incoming and outgoing momenta. Because the interaction conserves momentum, the sum of momenta on the incoming lines must be equal to those of outgoing lines:

$$\sum_{a=1}^4 c_a \delta_{j_a} = \mathbf{G}, \quad (48)$$

where \mathbf{G} is a reciprocal moiré lattice vector, the sum is over the four legs of the vertex, c_a is +1 for $\mathbf{m}_{j_a}^*$ (incoming) and -1 for \mathbf{m}_{j_a} (outgoing), and $j_a = 1, 2, 3$. At fourth order, there are five possible terms: m^4 , m^*m^3 , $m^{*2}m^2$, $m^{*3}m$ and m^{*4} . By explicitly checking all combinations of momentum transfer, the condition (48) allows for only the term $m^{*2}m^2$ to be non-vanishing, giving the fourth order contribution:

$$F_{(4)} = \frac{A\beta U}{2} \sum_{\mu\nu\gamma\eta} \sum_{jlmn} \frac{g_{jlmn}^{\mu\nu\gamma\eta}}{4} s_{\mu j}^* s_{\nu l}^* s_{\gamma m} s_{\eta n}, \quad (49)$$

where the tensor $g_{jlmn}^{\mu\nu\gamma\eta}$ is a function of four-particle electronic correlation functions. Instead of giving the explicit expression of the coefficients $g_{jlmn}^{\mu\nu\gamma\eta}$ we derive the symmetry allowed fourth order contributions given an order parameter of the form $s_{\mu j} = M_j U_{\mu}$. Observing that M_j transforms under the symmetries of the free energy as:

$$\begin{aligned} C_{3z} &: M_j \rightarrow M_{j+1}, \\ T &: M_j \rightarrow -M_j^*, \\ m_x &: M_1 \rightarrow M_1^*, m_x : M_2 \rightarrow M_3^*, \\ T_{\mathbf{R}} &: M_j \rightarrow M_j e^{i\delta_j \cdot \mathbf{R}}, \end{aligned} \quad (50)$$

where $T_{\mathbf{R}}$ indicates translation with respect to the moiré lattice vector \mathbf{R} , to fourth order in M_j the symmetry allowed terms are:

$$\begin{aligned} F &= r \sum_j |M_j|^2 + 2\omega \sum_j |M_j||M_{j+1}| \cos(\phi_j - \phi_{j+1}) + \frac{g_1}{4} \sum_j |M_j|^4 + \frac{g_2}{4} \sum_j |M_j|^2 |M_{j+1}|^2 \\ &+ g_3 \sum_j |M_j||M_{j+1}| \frac{|M_j|^2 + |M_{j+1}|^2}{4} \cos(\phi_j - \phi_{j+1}) + \frac{g_4}{4} \sum_j |M_j|^2 |M_{j+1}| |M_{j-1}| \cos(\phi_{j-1} - \phi_{j+1}) \\ &+ \frac{g_5}{4} \sum_j |M_j|^2 |M_{j+1}|^2 \cos(2\phi_j - 2\phi_{j+1}) + \frac{g_6}{4} \sum_j |M_{j-1}|^2 |M_j||M_{j+1}| \cos(2\phi_{j-1} - \phi_j - \phi_{j+1}). \end{aligned} \quad (51)$$

We do not exclude the possibility of different magnetic phases in strong coupling regimes where the coefficients g_i might be considerably renormalized.

V. PROPERTIES OF THE SKYRMION LATTICE

Real space magnetization pattern.— From the solution of Eqs. (39) and (40) we find a C_{3z} symmetric magnetic state. Correspondingly, the real-space expression of the order parameter is:

$$\mathbf{m}(\mathbf{r}) = \rho \sum_{\mu} U_{\mu} \mathbf{f}_{\mu}(\mathbf{r}). \quad (52)$$

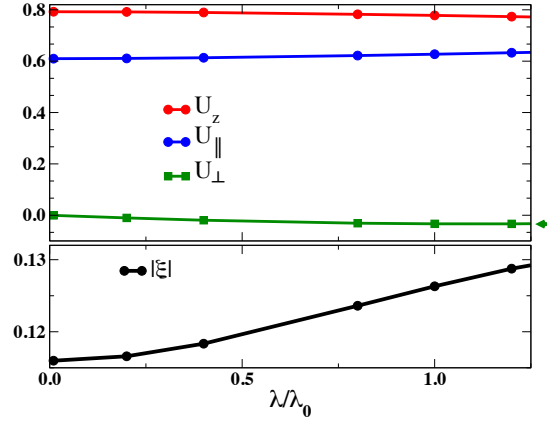


Figure 8. Evolution of the order parameter as a function of the hexagonal warping coefficient λ/λ_0 . Top panel: red, blue and green lines show the components U_z , $U_{||}$ and U_{\perp} . Bottom panel: evolution of $|M| = \sqrt{\sum_{\mu j} |s_{\mu j}|^2}$. The calculation has been performed setting $w = 30\text{meV}$, $L \simeq 17\text{nm}$, $U = 45\text{meV}$, $T = 2.26\text{K}$, $v_F = 2.55\text{eV}\text{\AA}$ and $\lambda_0 = 250\text{eV}\text{\AA}^3$.

In Eq. (52) we have introduced the basis functions:

$$\begin{aligned}
 \mathbf{f}_{||}(\mathbf{r}) &= 2 \sum_{j=1}^3 e_j \cos(\boldsymbol{\delta}_j \cdot \mathbf{r}), \\
 \mathbf{f}_{\perp}(\mathbf{r}) &= 2 \sum_{j=1}^3 (\mathbf{z} \times e_j) \sin(\boldsymbol{\delta}_j \cdot \mathbf{r}), \\
 \mathbf{f}_z(\mathbf{r}) &= 2 \sum_{j=1}^3 \mathbf{z} \sin(\boldsymbol{\delta}_j \cdot \mathbf{r}).
 \end{aligned} \tag{53}$$

We notice that the 120-xy order $\mathbf{f}_{||}(\mathbf{r})$ is longitudinal, $\nabla \times \mathbf{f}_{||}(\mathbf{r}) = 0$, while the out-of-plane and the spiral-xy orders are transverse, $\nabla \cdot \mathbf{f}_{\mu}(\mathbf{r}) = 0$ ($\mu = \perp, z$). In agreement with the character Table I we have $C_{3z}\mathbf{f}_{\mu}(\mathbf{r}) = \mathbf{f}_{\mu}(C_{3z}\mathbf{r})$. Moreover, $m_y\mathbf{f}_{||}(\mathbf{r}) = -\mathbf{f}_{||}(m_y\mathbf{r})$, $m_y\mathbf{f}_z(\mathbf{r}) = -\mathbf{f}_z(m_y\mathbf{r})$, while $m_y\mathbf{f}_{\perp}(\mathbf{r}) = \mathbf{f}_{\perp}(m_y\mathbf{r})$ with m_y acting on the space coordinate as $m_y : (x, y, z) \rightarrow (x, -y, z)$ while one the spin ones as $m_y : (a, b, c) \rightarrow (-a, b, -c)$. As a result, magnetic order parameters with finite U_{\perp} do not mix with order parameters that have finite $U_{||,z}$; the former corresponds to the Γ_1 representation, while the latter is the Γ_2 representation.

In addition, we find that $m_x\mathbf{f}_{\mu}(\mathbf{r}) = \mathbf{f}_{\mu}(m_x\mathbf{r})$, where $m_x : (x, y, z) \rightarrow (-x, y, z)$ in real space while $m_x : (a, b, c) \rightarrow (a, -b, -c)$ in spin space. By definition $T\mathbf{f}_{\mu}(\mathbf{r}) = -\mathbf{f}_{\mu}(\mathbf{r})$. Finally, under $C_{2z}T$, $C_{2z}T\mathbf{f}_{||}(\mathbf{r}) = \mathbf{f}_{||}(C_{2z}\mathbf{r})$, $C_{2z}T\mathbf{f}_z(\mathbf{r}) = \mathbf{f}_z(C_{2z}\mathbf{r})$ while $C_{2z}T\mathbf{f}_{\perp}(\mathbf{r}) = -\mathbf{f}_{\perp}(C_{2z}\mathbf{r})$. We conclude that the magnetic state Γ_2 is invariant under $C_{2z}T$. A finite spiral-xy component breaks m_y and $C_{2z}T$ but preserves C_{3z} and m_x .

Effect of the hexagonal warping term.— The hexagonal warping term $H_w(\mathbf{r})$ breaks m_y so that the two irreducible representations Γ_1 and Γ_2 are indistinguishable. As a result, the skyrmion lattice acquires a finite spiral-xy component $U_{\perp} \neq 0$. To quantify the effect of H_w , Fig. 8 shows the evolution of the order parameter obtained by solving the saddle-point equations (37) and (38) in the presence of hexagonal warping. In particular, the top panel of Fig. 8 shows the components U_{μ} (normalized so that $\mathbf{U}^T \cdot \mathbf{U} = 1$) as a function of the dimensionless quantity λ/λ_0 . We treat λ as a free parameter measured in units of $\lambda_0 = 250\text{eV}\text{\AA}$, the computed value in Bi_2Te_3 [1–3]. We observe a small but finite spiral-xy component in Fig. 8 which grows by increasing the ratio λ/λ_0 in agreement with the group-theoretical prediction. The bottom panel of Fig. 8 shows the magnetization density $|M|$ as a function of λ . Any distortion of the potential that breaks the mirror symmetry will also enhance the value of U_{\perp} . The detailed analysis of these effects is left to future studies.

Magnetoelectric effect.— The lack of space-inversion and time-reversal symmetry in skyrmion lattices results in a magnetoelectric multipole $\int d^2\mathbf{r} r_i m_j$ that in two-dimensions is a rectangular matrix with $i = x, y$ and $j = x, y, z$. The skyrmion lattice with $U_{\perp} = 0$ and transforming as the Γ_2 representation is odd under the mirror m_y symmetry. As a result, all components $\int d^2\mathbf{r} r_i m_j$ vanish except $\int d^2\mathbf{r} x m_z$ which is not constrained to be zero by the symmetries. A finite hexagonal warping term, or any term that breaks the mirror symmetry m_y , gives rise to a finite out-of-plane toroidal moment $\mathcal{T}_z = \int d^2\mathbf{r} \varepsilon_{ij} r_i m_j / 2$. On the other hand, $\mathcal{T}_x = \int d^2\mathbf{r} y m_z / 2$ vanishes as a consequence of m_x symmetry even in the presence of hexagonal warping, while \mathcal{T}_y is the only component which can be finite without

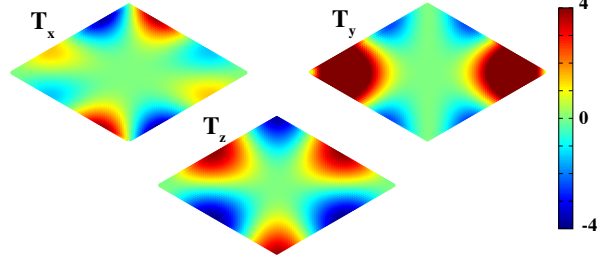


Figure 9. Components of the toroidal moment density $\mathcal{T}_i(\mathbf{r}) = \epsilon_{ijk}r_j m_k(\mathbf{r})/2$ in the magnetic moiré unit cell. The component \mathcal{T}_y is finite even for the m_y symmetric Γ_2 magnetic state. For $U_\perp \neq 0$, $\mathcal{T}_z \neq 0$, while \mathcal{T}_x is still vanishing due to m_x .

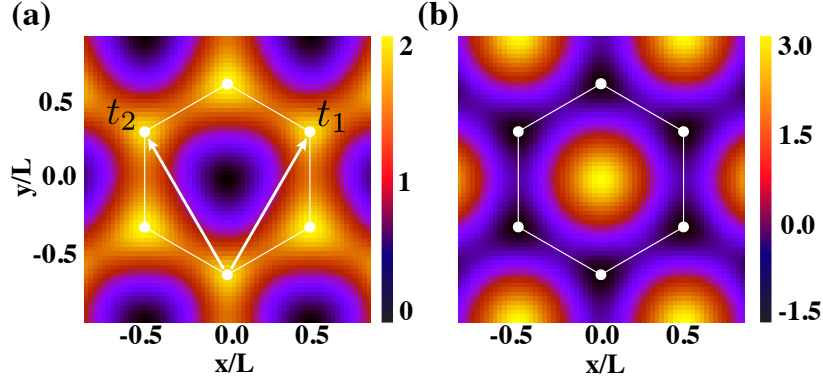


Figure 10. (a) Real-space probability distribution from the Bloch orbitals of $H_0(\mathbf{r})$ at \mathbf{K} for the first positive energy band (\mathbf{K}' gives the same density) and (b) moiré potential $w(\mathbf{r})$ in unit of w . The white line denotes the real-space unit cell and the white arrows denote the primitive vectors $\mathbf{t}_{1(2)} = L(\pm 1/2, \sqrt{3}/2)$. Position is measured in unit of $L = 20\text{nm}$, the plot has been obtained by setting $w/(v_F/L) = 1.54$ and $\lambda = 250\text{eV}\text{\AA}^3$.

any symmetry breaking. Fig. 9 shows the evolution of $\epsilon_{ijk}r_j m_k/2$ in the magnetic moiré unit cell. We leave to future work a detailed analysis of this effect.

VI. THE ORIGIN OF UNCONVENTIONAL MAGNETISM

Charge and spin density distribution at \mathbf{K} and \mathbf{K}' .— To develop intuition on the origin of the skyrmion lattice we study the real-space charge and spin distributions originating from the first band above charge neutrality at \mathbf{K} and \mathbf{K}' . The left panel in Fig. 10 shows the charge distribution, defined as:

$$\rho_{\mathbf{k}}(\mathbf{r}) = \mathbf{u}_{\mathbf{k}}^\dagger(\mathbf{r}) \cdot \mathbf{u}_{\mathbf{k}}(\mathbf{r}), \quad (54)$$

where $\mathbf{k} = \mathbf{K}, \mathbf{K}'$ and the Bloch function $\mathbf{u}_{\mathbf{k}}(\mathbf{r})$ at \mathbf{k} is given by:

$$\mathbf{u}_{\mathbf{k}}(\mathbf{r}) = \sum_{\mathbf{Q}} e^{-i\mathbf{Q}\cdot\mathbf{r}} \begin{pmatrix} u_{\mathbf{k}\mathbf{Q}\uparrow} \\ u_{\mathbf{k}\mathbf{Q}\downarrow} \end{pmatrix}. \quad (55)$$

We also depict the moiré superlattice potential in the right panel of Fig. 10. Comparing the two panels shows that the electron distribution is concentrated around the minima of the potential $w(\mathbf{r})$ and vanishes at the maxima of $w(\mathbf{r})$, as expected. We further introduce the quantity:

$$\sigma_{\mathbf{k},a}(\mathbf{r}) = \sum_{\sigma\sigma'} u_{\mathbf{k}\sigma}^*(\mathbf{r}) \sigma_{a,\sigma\sigma'} u_{\mathbf{k}\sigma'}(\mathbf{r}), \quad (56)$$

where $a = x, y, z$. Fig. 11 shows the real-space spin-texture originating from the Bloch wave functions at \mathbf{K} , the one at \mathbf{K}' is obtained by applying time-reversal symmetry. The topological spin pattern follows from the interplay between

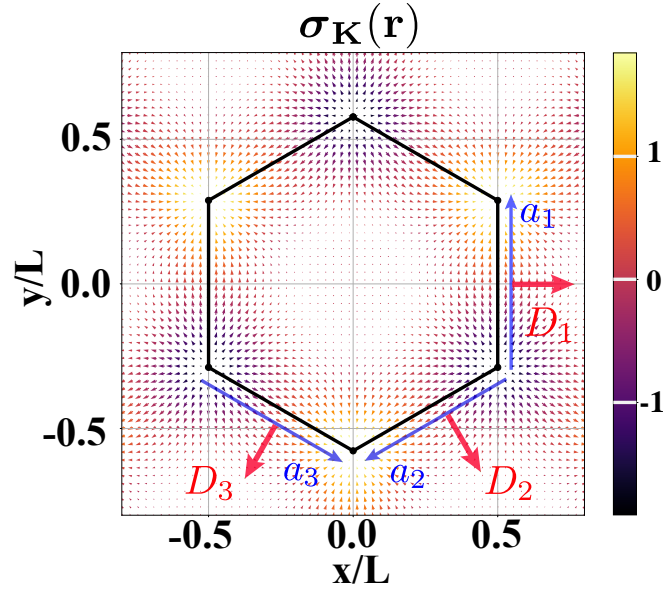


Figure 11. Real-space spin-textures of the Bloch eigenstates of $H_0(\mathbf{r})$ at \mathbf{K} for the first positive energy band. The spin-textures at \mathbf{K}' is related by time-reversal symmetry. The black solid line denotes the real-space unit cell, the blue arrows the vectors $\mathbf{a}_j = LC_{3z}^{j-1}\mathbf{y}/\sqrt{3}$ and the red ones the spin canting axis \mathbf{D}_j around whose the spin winds anticlockwise. The real space position is measured in units of $L = 20\text{nm}$, the plot has been obtained by setting $w/(v_F/L) = 1.54$ and $\lambda = 250\text{eV}\text{\AA}^3$.

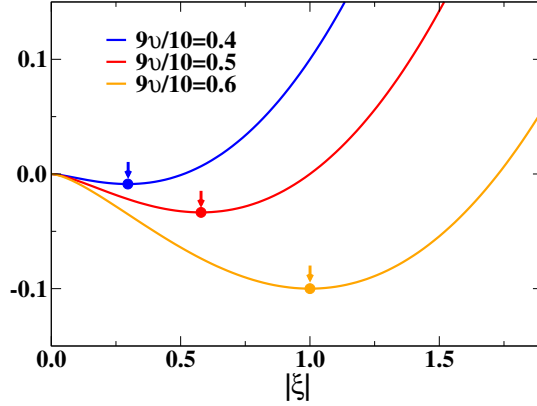


Figure 12. Free energy variation for a power-law divergent density of states at $T = 0\text{K}$. The arrows denote the position of the free energy minimum that describes a magnetic state. The position of the minimum depends on a single dimensionless parameter $v = CA^{5/3}/U$.

the intrinsic SOC of the TI surface and the underlying moiré lattice. In particular, the spin canting vector is related to the real-space translation $\Delta\mathbf{r}$ by $D_{\Delta\mathbf{r}} = (\mathbf{z} \times \Delta\mathbf{r})/|\Delta\mathbf{r}|$. Moving along the three edges $\Delta\mathbf{r} = \mathbf{a}_j = LC_{3z}^{j-1}\mathbf{y}/\sqrt{3}$ blue vectors in Fig. 11 connecting maxima of the charge distribution $\rho_{\mathbf{K}}(\mathbf{r})$, $\rho_{\mathbf{K}'}(\mathbf{r})$ shown in Fig. 10 the spin rotates anticlockwise around the axis \mathbf{D}_j . In the normal state the two valleys \mathbf{K} and \mathbf{K}' are equally occupied giving rise to a time-reversal symmetric state with vanishing magnetization. The skyrmion lattice state belonging to Γ_2 breaks the mirror symmetry m_y of \mathbf{K} and \mathbf{K}' . The resulting Hartree-Fock orbitals at Γ_m of the magnetic moiré Brillouin zone are eigenstates of the mirror symmetry m_x and correspond to a coherent superposition of the two valleys \mathbf{K} and \mathbf{K}' with opposite eigenvalues.

Energetics of the skyrmion lattice.—The electron interaction couples the two valleys and can give rise to a magnetic state which spontaneously breaks time-reversal symmetry. Using the free energy in Eq. (36) we now perform a simplified calculation that gives insight into the origin of the unconventional magnetic state discussed in the manuscript.

At fixed electron filling n varying the magnetic state with respect to the normal one yields the following variation

of the free energy (36):

$$\Delta F = \frac{U}{2} \sum_{\mu j} |s_{\mu j}|^2 - k_B T \sum_n \int \frac{d^2 \mathbf{k}}{\Omega_{\mathbf{k}}} \left[\log \left(1 + e^{-\beta \bar{\xi}_{n\mathbf{k}}} \right) - \log \left(1 + e^{-\beta \xi_{n\mathbf{k}}} \right) \right], \quad (57)$$

where $\bar{\epsilon}_{n\mathbf{k}}$ are the eigenvalues of the Hartree-Fock Hamiltonian (21), $\epsilon_{n\mathbf{k}}$ eigenvalues of $H_0(\mathbf{r})$ (1), while $\bar{\xi}_{n\mathbf{k}} = \bar{\epsilon}_{n\mathbf{k}} - \mu^*$ and $\xi_{n\mathbf{k}} = \epsilon_{n\mathbf{k}} - \mu$ with μ^* and μ chemical potentials that give the filling n . Eq. (57) becomes particularly simple in the limit of vanishing temperature. By introducing the density of states (DOS) $\rho(\epsilon) = \sum_n \int d^2 \mathbf{k} \delta(\epsilon - \xi_{n\mathbf{k}}) / \Omega_{\mathbf{k}}$ we have:

$$\Delta F = \frac{U}{2} \sum_{\mu j} |s_{\mu j}|^2 + \int^{<0} d\epsilon \epsilon [\bar{\rho}(\epsilon) - \rho(\epsilon)], \quad (58)$$

where $\bar{\rho}(\epsilon)$ and $\rho(\epsilon)$ are the DOS of the magnetic and the normal state, respectively, and the energy is measured with respect to the chemical potential. For simplicity we assume to be at the higher-order VHS where the density of states is $\rho(\epsilon) = C|\epsilon|^{-1/3}$ and we introduce an ultraviolet energy cutoff Λ . On the other hand, a finite magnetic order $s_{\mu j} = \xi U_{\mu} / \sqrt{3}$ splits the HOVHS and gives the DOS $\rho(\epsilon) = C(|\epsilon - A|M|^{-1/3} + |\epsilon + A|M|^{-1/3})/2$. By expanding the kinetic energy difference in Eq. (58) to the lowest order in $\delta = A|M|/\Lambda \ll 1$ we find:

$$\int_{-\Lambda}^0 d\epsilon \epsilon [\bar{\rho}(\epsilon) - \rho(\epsilon)] = C\Lambda^{5/3} \left[-\frac{9\delta^{5/3}}{10} + \mathcal{O}(\delta^2) \right]. \quad (59)$$

Thus, the free energy variation goes like

$$\frac{\Delta F}{U} \simeq \frac{|M|^2}{2} - \frac{9}{10} v |M|^{5/3}, \quad (60)$$

where we have introduced the dimensionless parameter $v = CA^{5/3}/U$. As shown in Fig. 12 the normal state $\xi = 0$ is unstable and the free energy minimum characterized by a finite magnetization $|M| = (3v/2)^3$. By using symmetry arguments we find that only the Γ_2 magnetic ordering, see Table I, couples \mathbf{K} and \mathbf{K}' and splits the VHS.

-
- [1] Y. L. Chen, J. G. Analytis, J.-H. Chu, Z. K. Liu, S.-K. Mo, X. L. Qi, H. J. Zhang, D. H. Lu, X. Dai, Z. Fang, et al., *Science* **325**, 178 (2009), <https://www.science.org/doi/pdf/10.1126/science.1173034>, URL <https://www.science.org/doi/abs/10.1126/science.1173034>.
- [2] D. Hsieh, Y. Y. Xia, D. Qian, L. A. Wray, J. H. Dil, F. Meier, J. Osterwalder, L. Patthey, J. G. Checkelsky, N. P. Ong, et al., *Nature* **460**, 1101 (2009), URL <https://doi.org/10.1038/nature08234>.
- [3] L. Fu, *Phys. Rev. Lett.* **103**, 266801 (2009), URL <https://link.aps.org/doi/10.1103/PhysRevLett.103.266801>.
- [4] N. F. Q. Yuan and L. Fu, *Phys. Rev. B* **101**, 125120 (2020), URL <https://link.aps.org/doi/10.1103/PhysRevB.101.125120>.
- [5] N. F. Q. Yuan, H. Isobe, and L. Fu, *Nature Communications* **10** (2019), ISSN 2041-1723, URL <http://dx.doi.org/10.1038/s41467-019-13670-9>.
- [6] A. Chandrasekaran, A. Shtyk, J. J. Betouras, and C. Chamon, *Phys. Rev. Research* **2**, 013355 (2020), URL <https://link.aps.org/doi/10.1103/PhysRevResearch.2.013355>.
- [7] D. Guerci, P. Simon, and C. Mora, *Higher-order van hove singularity in magic-angle twisted trilayer graphene* (2021), 2106.14911.
- [8] T. Wang, N. F. Q. Yuan, and L. Fu, *Phys. Rev. X* **11**, 021024 (2021), URL <https://link.aps.org/doi/10.1103/PhysRevX.11.021024>.
- [9] G. D. Mahan, *Many Particle Physics, Third Edition* (Plenum, New York, 2000).
- [10] C. Mudry, *Lecture Notes on Field Theory in Condensed Matter Physics* (WORLD SCIENTIFIC, 2014), <https://www.worldscientific.com/doi/pdf/10.1142/8697>, URL <https://www.worldscientific.com/doi/abs/10.1142/8697>.
- [11] E. Fradkin, *Field Theories of Condensed Matter Physics* (Cambridge University Press, 2013), 2nd ed.
- [12] A. Altland and B. D. Simons, *Condensed Matter Field Theory* (Cambridge University Press, 2010), 2nd ed.
- [13] T. Stauber, P. San-Jose, and L. Brey, *New Journal of Physics* **15**, 113050 (2013), ISSN 1367-2630, URL <http://dx.doi.org/10.1088/1367-2630/15/11/113050>.
- [14] D. Guerci, P. Simon, and C. Mora, *Physical Review B* **103** (2021), ISSN 2469-9969, URL <http://dx.doi.org/10.1103/PhysRevB.103.224436>.